Biofabrication

International Society for Biofabrication

PAPER

3D printed micro-chambers carrying stem cell spheroids and pro-proliferative growth factors for bone tissue regeneration

To cite this article: Jinkyu Lee *et al* 2021 *Biofabrication* **13** 015011

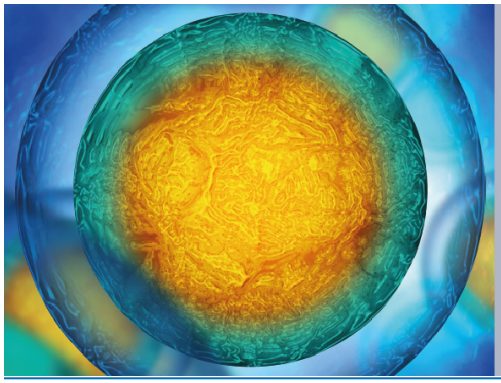

IOP Publishing Biofabrication 13 (2021) 015011 https://doi.org/10.1088/1758-5090/abc39c

Biofabrication

PAPER

RECEIVED
16 August 2020

REVISED
15 October 2020

ACCEPTED FOR PUBLICATION
21 October 2020

PUBLISHED
17 December 2020

3D printed micro-chambers carrying stem cell spheroids and pro-proliferative growth factors for bone tissue regeneration

Jinkyu Lee[1,2], Ji Min Seok[3], Seung Jae Huh[1,2], Hayeon Byun[1,2], Sangmin Lee[1,2], Su A Park[3] and Heungsoo Shin[1,2,4]

[1] Department of Bioengineering, Institute for Bioengineering and Biopharmaceutical Research, Hanyang University, Seoul 04763, Republic of Korea
[2] BK21 Plus Future Biopharmaceutical Human Resources Training and Research Team, Hanyang University, Seoul 04763, Republic of Korea
[3] Department of Nature-Inspired System and Application, Korea Institute of Machinery and Materials, Daejeon 34103, Republic of Korea
[4] Institute of Nano Science and Technology, Hanyang University, Seoul 04763, Republic of Korea

E-mail: psa@kimm.re.kr and hshin@hanyang.ac.kr

Keywords: 3D printing, dual growth factor delivery, osteoinductive spheroid, bone regeneration, micro-chamber

Supplementary material for this article is available online

Abstract

Three-dimensional (3D)-printed scaffolds have proved to be effective tools for delivering growth factors and cells in bone-tissue engineering. However, delivering spheroids that enhance cellular function remains challenging because the spheroids tend to suffer from low viability, which limits bone regeneration *in vivo*. Here, we describe a 3D-printed polycaprolactone micro-chamber that can deliver human adipose-derived stem cell spheroids. An *in vitro* culture of cells from spheroids in the micro-chamber exhibited greater viability and proliferation compared with cells cultured without the chamber. We coated the surface of the chamber with 500 ng of platelet-derived growth factors (PDGFs), and immobilized 50 ng of bone morphogenetic protein 2 (BMP-2) on fragmented fibers, which were incorporated within the spheroids as a new platform for a dual-growth-factor delivery system. The PDGF detached from the chamber within 8 h and the remains were retained on the surface of chamber while the BMP-2 was entrapped by the spheroid. *In vitro* osteogenic differentiation of the cells from the spheroids in the micro-chamber with dual growth factors enhanced alkaline phosphatase and collagen type 1A expression by factors of 126.7 ± 19.6 and 89.7 ± 0.3, respectively, compared with expression in a micro-chamber with no growth factors. *In vivo* transplantation of the chambers with dual growth factors into mouse calvarial defects resulted in a $77.0 \pm 15.9\%$ of regenerated bone area, while the chamber without growth factors and a defect-only group achieved $7.6 \pm 3.9\%$ and $5.0 \pm 1.9\%$ of regenerated bone areas, respectively. These findings indicate that a spheroid-loaded micro-chamber supplied with dual growth factors can serve as an effective protein-delivery platform that increases stem-cell functioning and bone regeneration.

1. Introduction

Three-dimensional (3D) printing of polymers or ceramics has been widely investigated for reconstructing bone tissue since the macro- and microscopic porosity, mechanical property, and size of the scaffolds can be customized to the shape of the fracture [1]. To accelerate tissue regeneration, a 3D printed scaffold can exploit combined approaches with multiple growth factors that enable induction of osteogenic differentiation and proliferation of stem cells [2]. For example, 3D printed beta tricalcium phosphate and polycaprolactone (PCL) scaffolds loaded with vascular endothelial growth factor (VEGF) and bone morphogenetic protein 2 (BMP-2) demonstrated rapid tissue infiltration of sheep spinal defect sites and increased bone regeneration in rabbit tibia defects, respectively, following implantation [3]. In addition, PCL scaffolds loaded with poly(lactic-co-glycolic) acid (PLGA) microparticles encapsulating BMP-2, VEGF, and platelet-derived growth factor (PDGF) significantly enhanced bone regeneration on

the outer regions of a defect after being implanted in an ovine tibia defect [4]. Despite promising regenerative outcomes using growth factors that stimulate migration and differentiation of host cells within implanted scaffolds, uncontrolled rapid release of growth factors, abnormal ectopic bone formation, limited bone maturation on the center of scaffolds, and connective tissue ingrowth hinder further development and application of these strategies [5, 6].

An alternative approach involves stem cells and 3D printed scaffolds that can participate in bone formation, for examples, 3D printed bioceramic scaffolds seeded with pre-differentiated bone marrow stem cells (BMSCs) [7], PLGA scaffolds with pre-MC3T3-E1 osteoblasts [8], and collagen scaffolds with osteogenic gene-transfected BMSCs [9] enhanced *in vitro* osteogenic cytokine secretion, cell viability, and *in vivo* osseointegration between host tissue and implanted materials. However, low seeding efficiency caused by the highly porous structure of scaffolds, even with a relatively large number of cells (10^4 ~ 10^7 for a single scaffold), cell death or detachment from the surface of scaffolds during surgical processes, and the potential elimination of pre-differentiated cells by immune rejection have been reported [10, 11]. A bio-printing method may be able to deliver cells that address these problems. For example, BMSCs, human mesenchymal stem cells (hMSCs), and MG63 osteoblastic cells have been suspended in agarose or gelatin solution to print scaffolds, demonstrating positive results for *in vitro* osteogenic cytokine secretion, differentiation of stem cells, and homogeneous *in vivo* delivery of cells, with minimal cell loss, and protection from macrophage-driven phagocytosis [12, 13]. However, bio-printed scaffolds for *in vivo* bone regeneration suffer from several drawbacks, including weak mechanical strength of printed hydrogels, which restricts robust bone ingrowth, potential post-printing cell damage, time-consuming processes for optimizing bio-printing conditions, and diffusional limitation of growth factors to entrapped cells [14].

Three-dimensional cellular spheroids formed by spontaneous assembly of suspended cells have attracted a great deal of attention in regenerative medicine as they offer unique biological properties relative to two-dimensional cultured cells, including strong cell–cell, cell–extracellular matrix (ECM) interactions, enhanced paracrine signaling, and high growth-factor secretion [15]. For example, spheroids prepared from MSCs and adipose-derived stem cells enhanced differentiation potential in the presence of osteogenic or chondrogenic media, and have been used to regenerate bone, cartilage, and subchondral bone *in vivo* [16, 17]. However, the implantation of spheroids into a bone defect can cause uncontrolled localization or heterogeneous distribution, limiting bone formation with immature lamellar structure formation [18]. Encapsulation of spheroids within hydrogels and arrangements of spheroids with needles, commercialized as the Kenzan method can partially mitigate problems associated with delivery of spheroids [19]. These methods effectively restrict the movement of transplanted spheroids and retain them within a desirable region. However, diffusion limitations within hydrogels, limited proliferation of cells from condensed large-cell constructs, weak mechanical properties, limited mineralization, and condensation of spheroids continue to limit implementation of the technology [20, 21]. Recently, spheroids were placed within pores of 3D printed structures to prevent them from aggregating. The positioning of spheroids within a 3D structure enhanced migration, proliferation, and viability of the cells, however, effective delivery of instructive signals into cells within the spheroids has proved difficult due to the presence of densely arranged cell-cell and cell-ECM binding surfaces [22, 23], which limit diffusion, and successful application of these approaches *in vivo* has yet to be reported. For example, Kelly *et al* developed a 3D printed PCL scaffold loading mesenchymal stromal cell spheroids, and the spheroids showed stable retention on the scaffold while showing enhanced *in vitro* chondrogenic differentiation although the study was limited to *in vitro* works and the *in vivo* efficiency of the proposed concept was not fully demonstrated [24].

In this study, we combined 3D printed scaffolds and spheroids of hADSCs with multiple-growth-factor delivery. The 3D printed scaffolds served as carriers of spheroids within each micro-chamber and were able to deliver a pro-angiogenic growth factor to the spheroids. The spheroids were prepared with engineered fibers coated with an osteoinductive factor to address diffusion limitations. First, we coated the surface of 3D printed micro-chambers with PDGF to improve the interaction and migration of cells from the spheroids, and then incorporated BMP-2–immobilized fibers within the spheroids during spheroid fabrication. Next, the spheroids were positioned in each micro-chamber, and *in vitro* viability, proliferation, and osteogenic differentiation of stem cells were studied. Finally, bone regeneration *in vivo* was examined with using a mouse calvarial defect model.

2. Methods

2.1. Materials

Poly(ι-lactic acid) (PLLA) (5.7–8.5° dL g^{-1} inherent viscosity, Mn 350 000–500 000 Da) was purchased from Samyang (Seoul, Korea). Dopamine hydrochloride, epigallocatechin gallate (EGCG), bis-tris, anti-mouse/rabbit immunoglobulin G (IgG) biotin conjugate, and Alizarin Red S were obtained from Sigma (St. Louis, MO, USA). Magnesium chloride hexahydrate was supplied by JUNSEI (Tokyo, Japan).

For cell cultures, hADSCs, basal medium, growth supplements, and L-glutamine were purchased from Invitrogen StemPro (Carlsbad, CA, USA). Penicillin/streptomycin (P/S) was obtained from Wisent (St. Bruno, QC, Canada), and phosphate-buffered saline (PBS) and its ion-free version, Dulbecco's phosphate-buffered saline (DPBS), were purchased from Welgene (Gyeongsan, Korea). For *in vitro* experiments, p-nitrophenyl phosphate, isopropyl alcohol, tris-HCl, and micro bicinchoninic acid (BCA) kits were purchased from Sigma, EMD Millipore (Burlington, MA, USA), Alfa Aesar (Haverhill, MA, USA), and Thermo Scientific (Heysham, UK), respectively. Quant-iT PicoGreen dsDNA assays were obtained from Invitrogen (Carlsbad, CA, USA) and hematoxylin and eosin (H&E) solution was purchased from BBC Biochemical (Mount Vernon, MA, USA). The growth factors PDGF and BMP-2 and each protein-related enzyme-linked immunosorbent assay (ELISA) were obtained from PeproTech (Rocky Hill, NJ, USA). A live-and-dead assay kit, fluorescein isothiocyanate (FITC)-streptavidin, and mounting medium with diamidino-2-phenylindole (DAPI) were obtained from Molecular Probes (Eugene, OR, USA), eBioscience (San Diego, CA, USA), and Vector Laboratories (Burlingame, CA, USA), respectively. Primary antibodies of OCN and OPN were purchased from Abcam (Cambridge, UK).

2.2. Preparation and characterization of PDGF-coated PCL micro-chambers

The micro-chambers were fabricated using a 3D printer constructed at the Korea Institute of Machinery and Materials (KIMM), consisting of an x-y-z translation stage, dispenser, and heating/compression controller. Before 3D printing procedure, PCL pellets (Mn 40 000–50 000 Da, cat. 704 105, Sigma-Aldrich) were melted in a stainless-steel barrel at 100 °C. After preparation of melted PCL in the barrel, the 3D printing was performed with 1 μm resolution according to the designed printing path using a laboratory-made software program [25]. Each strand in the chamber was designed 200 μm in diameter and the distance between strands was 300 μm for the first layer, and 800 μm for the second to the 10th layer to form square pores. The chamber was a 5 mm (x-axis) $\times$ 5 mm (y-axis) $\times$ 1 mm (z-axis) cuboid shape with layer-by-layer stacking. The precision nozzle with the inner diameter of 200 μm was prepared for printing the original design of the strand. After the modeling of the chamber, the melted PCL was printed with the designed path and the regulated velocity of the printing head as well as pneumatic pressure of the controller. The 3D printed micro-chambers were optimized several times with the correction of the shape, strand size, and distance between strands through the change of G-code in the program after optical microscope inspection. The printing conditions were optimized to fabricate within a few minutes per sample as suitable to the original design of the chamber by using above procedure to 180–200 mm min^{-1} of velocity and 475–500 kPa of pressure. All processes were carried out on a sterilized bench at room temperature. The exact scale of the synthesized micro-chamber were measured by calipers as 5.1 $\pm$ 0.0 mm (x-axis), 5.1 $\pm$ 0.0 mm (y-axis), and 1.0 $\pm$ 0.0 mm (z-axis) (figure S1(A) (stacks.iop.org/BF/13/015011/mmedia)). The diameter of strand was 0.2 $\pm$ 0.0 mm, and the width and length of one well were 0.8 $\pm$ 0.0 and 0.8 $\pm$ 0.0 mm, respectively (figure S1(B)).

To coat the PDGF, each 3D printed micro-chamber was immersed in 1 mg ml^{-1} of EGCG buffer (600 mM of magnesium chloride, and 100 mM bis-tris in distilled water (DW) at pH 7 and 37 °C) for 1, 2, 4, and 6 h. The samples were then immersed with the same EGCG buffer and 500 ng of PDGF for 1, 2, and 4 h. The surface morphologies of uncoated, EGCG-coated (for 4 h) (E-PCL), and PDGF-coated (for 4 h) PCL micro-chamber (PE-PCL) were observed using field-emission scanning electron microscopy (FE-SEM) (Hitachi S 4800 FE-SEM, HITACHI; Tokyo, Japan). For SEM imaging, the samples were dehydrated in the 37 °C vacuum desiccator for 24 h, and attached on SEM holder by carbon tape. The samples were then coated with platinum by ion sputter (6 nm s^{-1}, 10–15 nm thickness). The surface hydrophilicity of each sample was investigated by dipping the chamber in DW. The amount of polyphenol on the surface was analyzed using Folin and Ciocalteu's assay (Sigma). Briefly, the sample was pre-wetted with 200°ml of DW and mixed with the reagent solution, and then mixed with 600 μl of 2% sodium carbonate solution for 1 h with agitation. The optical density at a wavelength of 760 nm was observed by spectrometer (Varioskan LUX, Thermo Scientific; Waltham, MA, USA). The surface chemical composition of the chambers was characterized by high-resolution x-ray photoelectron spectra (Theta Probe Base System, Thermo Scientific; Waltham, MA, USA). The amount of PDGF on the chamber surface was quantified by an indirect method: the amount of PDGF in the supernatant of each coating condition was quantified by a PDGF ELISA kit, and the value was deducted from the initial amount of PDGF to calculate the amount of PDGF coated on the surface. The PE-PCLs were then incubated in physiological conditions (37 °C, PBS, rotation) for 28 d to measure the detachment of PDGF. The topographical mapping and the roughness of surface of PCL, E-PCL, and PE-PCL was measured by atomic force microscopy (AFM) (XE-100, Park-System, Korea) with non-contact mode at a scanning area of 5 $\times$ 5 μm^2.

2.3. Preparation of hADSC spheroids with engineered fibers

The hADSCs were cultured in a growth medium of the basal medium with 2% fetal bovine serum (FBS),

1% P/S, and 1% L-glutamine under standard culture conditions (5% CO_2 and 37 °C). Cells at passage number 4 or 5 were used throughout the experiments and the medium was refreshed every 2 d. Stem cell spheroids were prepared as described in our previous publications [26, 27]. First, aligned PLLA nanofiber sheets were prepared by electrospinning (5°ml h^{-1}, 23 G needle, 12–14 keV) using 10°ml of 4% PLLA solution in dichloromethane and trifluoroethanol (8:2, v/v). The electrospun sheet was subsequently chopped into small pieces and dipped in a 10% ethylenediamine solution at a ratio of 9:1 in isopropyl alcohol (IPA) (v/v) for 30 min at 200 rpm on a rotator for fragmentation of long fibers by aminolysis. The FFs were then collected by centrifugation at 3000 rpm for 5 min and washed with IPA, ethanol, and DW. For polydopamine coating on the surface to improve cell adhesion, the fibers were immersed in a 2 mg ml^{-1} dopamine solution (tris-HCl buffer, pH 8.5) for various times, and the amount of amine groups from the resulting PD-FFs was quantified by micro-BCA assay. We used fibers coated for 20 min following sterilization with 70% ethanol and ultraviolet light for spheroid formation. To prepare spheroids of stem cells and fibers, 40 000 trypsinized cells were placed in a 0.2 ml tube with 100 μl of growth media and 10 μg of PD-FFs, and allowed to spontaneously form a spheroid for 24 h (denoted as PS). The spheroids were then moved onto a 96-well ultra-unattached cell culture plate (SPL Life Science; Pocheon, Korea) for further *in vitro* culture.

The morphology of the spheroids was analyzed by FE-SEM after fixation (immersion in 4% paraformaldehyde for more than 20 min) and freeze-drying. The size of the spheroids was calculated from images taken by a phase contrast microscope (CKX41, Olympus; Tokyo, Japan) after 24 h and 7 d of culture. For histological analysis, spheroids cultured for 24 h were fixed in 4% paraformaldehyde for 20 min and frozen in an optimal cutting temperature (OCT) compound at −80 °C overnight, and then cross-sectioned using a cryo-microtome (Cryostat Cryocut, Leica Biosystems GmbH; Wetzlar, Germany). The sectioned specimen was dipped in sequential hydration steps from 70% to 100% ethanol, and running water. The specimen was then stained with hematoxylin for 2 min, rinsed with water, and stained again with eosin for 8 min. The H&E-stained sample was dehydrated following reverse steps of hydration, and then mounted. For the DNA assay, the spheroids were collected after 1 and 7 d of culture, lysed in 100 μl of a radioimmune precipitation assay lysis buffer (150 mM NaCl, 1% Triton X-100, 1% sodium deoxycholate, 0.1% SDS, 150 mM Tris, pH 7.2), and reacted with working reagents from the Quant-iT Picogreen dsDNA assay kit. Fluorescent intensity was measured using a spectrophotometer (Varioskan LUX, Thermo Scientific; Waltham, MA, USA) with excitation and emission wavelengths of 480 and 520 nm, respectively.

2.4. *In vitro* culture of stem cell spheroids within 3D printed micro-chambers

For *in vitro* culturing, we manually placed individual spheroids (PS) within each well of the micro-chamber coated with only EGCG (E-PCL-PS) and PDGF-EGCG (PE-PCL-PS). The loading of spheroids was manageable by using a pipette, and thus, the spheroids were manually transferred to each well of micro-chamber one-by- one while being monitored by the microscope. The phase contrast images (figure 3(A)) and TUNEL assay (figure 4(F)) demonstrated that the dissociated cell debris or fibers, and apoptotic cells were rarely found because the size of spheroid was small enough to safely penetrate the end of tip. Furthermore, the loading efficiency of spheroids was 100% because even if the spheroids were miss-loaded to the undesired well or out of the chamber, the spheroids were easily sucked out and re-loaded onto the proper well. As a control, four spheroids were placed on an ultra-unattached culture plate and allowed to assemble into a larger aggregate (IPS). The samples were then cultured for 14 d in the growth medium and the morphologies were analyzed by optical microscope and FE-SEM. The PE-PCL-PS was vertically sectioned (figure 4(A)) to demonstrate cell distribution within the well. For H&E staining, the IPS group was treated by the OCT embedding method while the micro-chambers cultured with spheroids were embedded in paraffin; samples were fixed in 4% paraformaldehyde within a cassette and tightly immobilized, dehydrated by being immersed in graded concentrations of ethanol (70%, 90%, four times at 100%, and xylene), hardened in a paraffin solution as a block while cooling (70 °C–4°C), and sliced horizontally (figure 4(C)) into 10 μm section using a microtome (Leica Biosystems GmbH; Wetzlar, Germany). The sections were sequentially deparaffinized in xylene, hydrated, and stained with an H&E solution. Cell distribution within the well after culturing for 7 d was quantitatively analyzed by staining the nuclei with DAPI under a confocal microscope (TCS SP5, Leica; Wetzlar, Germany). The terminal deoxynucleotidyl-mediated nick-end labeling (TUNEL), DNA, and 3-(4,5-dimethylthiazol-2-yl)-2,5-diphenyl-2 H-tetrazolium bromide (MTT) assays were also performed. Briefly, the TUNEL assay used the Apop Tag Fluorescein *In Situ* Apoptosis Detection Kit (Merk Millipore; Burlington, MS, USA) to horizontally cross-section specimens following the histological process, and TUNEL-positive nuclei were captured by a fluorescence microscope (TE 2000, Nikon; Tokyo, Japan) and their numbers counted. The samples for DNA assays were subjected to the aforementioned method. For the MTT assay, the samples were incubated with 40 μl of MTT solution (5 mg ml^{-1} in DPBS) and 500 μl of serum-free medium for 2 h at 37 °C, and the formazan salts generated during the incubation were then dissolved in 400 μl of dimethyl sulfoxide for 10 min.

Absorbance at 550 nm was measured using the spectrometer.

2.5. Preparation of hADSC spheroids with fibers immobilizing BMP-2

PD-FFs were used to immobilize BMP-2 (100, 300, and 500 ng ml^{-1} of BMP-2 in Tris-HCl buffer with agitation for 24 h at 4 °C, and denoted as BF10, BF30, and BF50, respectively). Retention of BMP-2 on the surface was confirmed by incubation of the BMP-2–immobilized fibers under physiological conditions (37 °C, PBS, rotation) for up to 28 d. The immobilized amount of BMP-2 was quantified by a BMP-2 ELISA kit using the procedure applied to PDGF quantification. Spheroids incorporating fibers immobilized with BMP-2 (BPS) were then prepared following a previously described procedure for PS. The viability of hADSCs within the spheroids after 24 h was analyzed by staining with calcein AM (1:1000) and ethidium homodimer (1:500) in DPBS, and cells were observed with a confocal microscope. The DNA contents from each spheroid (PS and BPS) cultured for 1, 4, and 7 d were compared. The spheroids were cultured for 14 d in a growth medium, and analyzed for osteogenic differentiation of hADSCs using Real-time quantitative polymerase chain reaction (RT-qPCR) amplification (StepOnePlus Real-Time PCR System, Applied Biosystems; Foster City, CA, USA) and a calcium assay. The mRNA of each spheroid was extracted using RNeasy Mini Kit (Qiagen; Hilden, Germany) with RNA purity confirmed using NanoDrop 2000 (Thermo Scientific; Waltham, MA, USA). The cDNA was then synthesized by adding 1 μg of mRNA into a cDNA polymerization kit (Maxime RT PreMix kit, iNTRON Biotechnology; Seongnam, Korea) with a total volume of 20 μL in diethyl pyrocarbonate (DEPC)-treated water. Subsequently, 2 μl of the cDNA was mixed with SYBR Green Premix (Takara; Tokyo, Japan) and primers (COSMO Genetech; Seoul, Korea) with specific sequences, which were runt-related transcription factor 2 (RUNX2): forwards, 5′-GCA GTT CCC AAG CAT TTC AT-3′, reverses, 5′-CAC TCT GGC TTT GGG AAG AG-3′; osterix (OSX): forwards, 5′-TAA TGG GCT CCT TTC ACC TG-3′, reverses: 5′-CAC TGG GCA GAC AGT CAG AA-3′, osteopontin (OPN): forwards, 5′-TGA AAC GAG TCA GCT GGA TG-3′, reverses, 5′-TGA AAT TCA TGG CTG TGG AA-3′; osteocalcin (OCN): forwards, 5′-GTG CAG AGT CCA GCA AAG GT-3′, reverses, 5′-TCA GCC AAC TCG TCA CAG TC-3′; and the housekeeping gene GAPDH: forwards, 5′-GTC AGT GGT GGA CCT GAC CT-3′, reverses, 5′-TGC TGT AGC CAA ATT CGT TG-3′. The mixture was then examined by RT-qPCR for 40 cycles by melting at 95 °C for 15 s, annealing at 60 °C for 60 s, and extending at 62 °C. The relative fold changes in gene expression from BPS were normalized by that from the PS group. For the calcium assay, the calcium ions deposited in each spheroid were extracted by incubating them in 100 μl of a 0.6 N HCl buffer for 24 h at 37 °C. Next, 10 μl of the extracted supernatant was mixed with a working reagent from the QuantiChrom calcium assay kit (Bioassay Systems; Hayward, CA, USA), and the optical density from each sample was measured using a spectrometer at 612 nm and normalized by DNA content. Deposition of calcium minerals was visualized by fixing the cross-sectioned spheroids with 4% paraformaldehyde and then immersing them in an Alizarin Red S working solution (2% in DW with pH 4.2) for 2 min following washing with PBS and mounting. The images were captured by the optical microscope. All the sample codes of spheroids used in the study was summarized in table 1.

Table 1. The samples codes for spheroids used in the study.

Sample code	BMP-2 immobilized fiber	Integration of spheroids
PS	X	X
BPS	O	X
IPS	X	O
IBPS	O	O

2.6. *In vitro* osteogenic differentiation of stem cell spheroids within 3D printed micro-chambers

The spheroids were placed within each well of micro-chambers as previously described. Sample conditions of four groups are described in table 2. The samples were cultured for 14 d culturing under growth medium, lysed in Trizol reagent (Life Technologies; Carlsbad, CA, USA), and mRNA sequences were extracted. The osteogenic gene expression was investigated using RT-qPCR amplification. The expression of additional genes of alkaline phosphatase (ALP) (primer sequence: forwards, 5′-CCA CGT CTT CAC ATT TGG-3′, reverses, 5′-AGA CTG CGC CTG GTA GTT-3′) and collagen type 1A (Col1a) (primer sequence: forwards, 5′-CCG GAA ACA GAC AAG CAA-3′, reverses: 5′-AAA GGA GCA GAA AGG GCA-3′) was also analyzed. The samples were embedded in paraffin and sectioned horizontally to conduct immunohistochemistry (IHC) staining for OCN and OPN. The sectioned specimens were fixed with 4% paraformaldehyde and reacted with anti-OCN and anti-OPN solution (1:100 in blocking buffer, 0.1% Tween-20, and 5% FBS in PBS) for 24 h at 4 °C, followed by reactions with anti-mouse/rabbit IgG biotin-conjugated secondary antibodies (1:100 in PBS) for 1 h at 37 °C and FITC-conjugated streptavidin tertiary antibodies (1:100 in PBS) for 1 h at 37 °C. The specimens were then mounted with a medium containing DAPI on glass slides and observed through a fluorescence microscope. The OCN-and OPN-positive nuclei were counted from more than five samples in each group and the ratio per DAPI stained nuclei was calculated.

Table 2. The sample codes for micro-chamber incorporating spheroids used in the study.

Sample code	EGCG coating	PDGF coating	PS loading	BPS loading
E-PCL	O	X	X	X
PE-PCL	O	O	X	X
E-PCL-PS	O	X	O	X
PE-PCL-PS	O	O	O	X
E-PCL-BPS	O	X	X	O
PE-PCL-BPS	O	O	X	O

The samples were horizontally sectioned to visualize ALP and calcium deposition. First, the samples were treated with fixation solution composed of a citrate concentration (0.8%), acetone (60%), and DW (39.2%) for 30 s, and washed with DW. The samples were then treated with an alkaline-dye mixture composed of Fast Blue RR capsules (Sigma) dissolved in DW (96%) and a 4% naphthol AS-MX phosphate alkaline solution (Sigma) for 30 min with agitation. For calcium-mineral staining and quantification, the samples were subjected to the Alizarin Red S staining and calcium assay methods. The stained samples were observed through the optical microscope.

For the mechanical compression test of the PCL and PE-PCL-BPS, the chambers were evaluated from a universal testing machine (RB302 Microload, R&B, Korea). The compressive test was performed with a 50 kgf and displacement rate of 10 mm min^{-1} at the room temperature to obtain the stress–strain curves. The compressive modulus was determined based on the slope of the linear region of the stress–strain curve.

2.7. *In vivo* mouse calvarial defect model

For *in vivo* implantation, the design of a PCL microchamber was modified to a circular shape with a 4 mm radius while the other parameters were consistent. Nine spheroids were placed within each microchamber and cultured *in vitro* for 48 h to inhibit the escape of spheroids from the chamber. The samples were then implanted into mouse calvarial defects (critical sized defect [CSD]: 4 mm diameter of circular shape, five-week-old, female, Institute for Cancer Research species (Narabiotech, Seoul, Korea) ($n = 6$) [28]). Animal care and experiments were approved by the Institutional Animal Care and Use Committee of Hanyang University (approval number 2019-0173A). For the control, nine hADSC spheroids prepared with fibers immobilized with BPS were transplanted without micro-chamber support (IBPS). Before surgery, each mouse was anesthetized with 150 μl of zoletil (60 mg kg^{-1}) and rompun (20 mg kg^{-1}), and the head fur was shaved off. Skin above the calvarial bone was incised after sterilization with 70% ethanol, and a CSD was created using a surgical trephine drill. The pre-cultured samples were transplanted onto each defect site and the incised skin was sutured following treatment with povidone-iodine to prevent infection. The mice were sacrificed by CO_2 suffocation after eight weeks and the full calvarial bones were collected, fixed with 10% formalin, and stored at 4 °C for future analysis. The bone specimens were analyzed by microcomputed tomography (micro-CT) (Skyscan1176 Bruker microCT) (Billerica, MA, USA) under fixed conditions (x-ray, 80 kV, 124 μA). The 3D images were created and the results of regenerated bone quantity were examined using 3D viewer, Ctan, and CTvol software from Bruker micro-CT. Bone area was calculated using Adobe Photoshop CS6 software by measuring the ratio of regenerated area to defect area from the 3D images. The ratio of the regenerated bone volume (BV/TV) was calculated automatically by Ctan after setting the region of interest. The TV indicated a fixed value covering all of the regenerated bone places and adjusted equally for all samples.

For histological analysis, the samples were decalcified with RapidCal solution (BBC Biochemical; Mount Vernon, WA, USA), re-fixed, dehydrated with graded concentrations of ethanol (70%, 90%, and four times at 100%), xylene, and embedded in paraffin. The sliced 6 μm samples were deparaffinized, hydrated, and stained with Goldner's trichrome staining solution. For Von Kossa staining, the samples were treated with a 2% silver nitrate solution under a 60 W lamp and 5% sodium thiosulfate, sequentially. The stained samples were dehydrated, mounted, and observed through the optical microscope. The ECM was characterized as light green in color and minerals on tissues were stained black. Staining for OPN/DAPI was also performed on sectioned specimens following the aforementioned IHC procedure of spheroids and observed with the fluorescent microscope.

2.8. Statistical analysis

All quantitative data were calculated and expressed as means ± standard deviation. For statistics, GraphPad Prism 5 software (La Jolla, CA, USA) was used to perform one-way analysis of variance (ANOVA) with either Tukey's honestly significant difference test (for more than two variables) or Student's t-test (for two variables). Significance was denoted at a value of $P < 0.05$, and all values were calculated from at least triplicate samples ($n \geq 3$). All experiments were independently repeated at least three times.

3. Results

3.1. Characterization of 3D printed micro-chambers and PDGF immobilization

A scheme involved in EGCG-mediated PDGF coating on the surface of PCL micro-chamber is depicted in figure 1(A), and demonstrated the color of chamber was changed into dark brown after coating. The chamber was composed of nine layers with strands 200 μm in diameter with homogeneous 800 μm gaps between them stacked on the first ejected layer, which was designed to have an additional strand with 300 μm intervals to prevent spheroid leakage (figure 1(B)). The SEM images from the tilted side of the chamber confirmed the structure of layers without apertures between them, strands with homogeneous intervals with consistent cubic spaces, and supporting strands aligned at regular distances (figure 1(C)). The chambers without coating, with EGCG coating, and both PDGF and EGCG were nominated as PCL, E-PCL, and PE-PCL, respectively. The surface following the coating process was fully covered by EGCG; such a difference was not observed after PDGF coating (figure 1(D)). The surface of the PCL micro-chamber became more hydrophilic after coating (figure 1(E)). The amount of EGCG on the surface of the micro-chamber increased depending on the coating time, although it was saturated after 4 h at 57.1 $\pm$ 6.2 ng mm^{-2} (figure 1(F)). As shown in an XPS spectrum, Mg1s (1304.08 eV) and Cl2p (198.9 eV) peaks appeared after EGCG coating and the N1s (399.08 eV) peak was detected after coating with PDGF (PE-PCL) (figure 1(G)). The immobilization efficiency of PDGF was 89.0% $\pm$ 2.1%, 70.6% $\pm$ 2.2%, and 45.0% $\pm$ 4.7% when the chamber was treated with 1 mg mL^{-1} of EGCG and 500 ng mL^{-1} of PDGF for 1, 2, and 4 h, respectively (figure 1(H)). The weakly coated PDGF detached within 8 h (figure 1(I)), and the other proteins remained on the surface of micro-chamber for 28 d (figure 1(J)). After 4 h of coating, 52.6% $\pm$ 1.7% of PDGF was released within 8 h and 99.1% $\pm$ 0.1% of the remaining PDGF was retained for 28 d.

3.2. Preparation of hADSC spheroids with engineered fibers

A scheme for preparing PS incorporating hADSC and PD-FFs is presented in figure 2(A). The amount of amine groups from polydopamine reached a saturation point after 20 min at 3.2 $\pm$ 0.1 μg μg^{-1} of fiber (figure 2(B)). SEM images of spheroid and its inside proved that a stable sphere formed without loss of cells or fibers after 24 h and the fibers were homogeneously mixed with cells inside of spheroid (figure 2(C)). Similarly, a H&E staining also showed that the cells and fibers were homogeneously distributed within the spheroids and the cells exhibited a well-assembled and integrated structure (figure 2(D)). The size and DNA contents of PS slightly decreased after 7 d, possibly due to stronger interactions of cells with fibers over time (figures 2(E) and (F)).

3.3. *In vitro* culture of stem cell spheroids within 3D printed micro-chambers

Following *in vitro* culturing of spheroids within 3D printed micro-chambers, phase contrast images showed that the spheroids were positioned stably within each hole of the micro-chamber (E-PCL-PS and PE-PCL-PS), maintaining a spheroidal shape while the spheroids were spontaneously and rapidly attached with other spheroids in the absence of a micro-chamber (IPS) within 24 h (figure 3(A)). Histological staining clearly showed that the borders of each spheroid began to fuse together, and the cells in spheroids at the micro-chamber migrated toward the strands of the chamber (figure 3(B)). The SEM images also revealed that a void space generated by the curvature of each spheroid was not detected in the IPS group because of the fusion. However, cells within spheroids inside the micro-chamber formed extended filopodia, sprouting toward the strands after 24 h of culturing on E-PCL and PE-PCL (figure 3(C)). After 14 d of culture, the IPS showed that the spheroids formed one large aggregate by complete fusion of each spheroid while the E-PCL-PS and PE-PCL-PS showed that the cells from each spheroid proliferated and migrated to fully cover the holes of the chamber (figure 3(D)). Histological stained images showed that the borders of the spheroids completely disappeared after 14 d, while individual spheroid shapes were still found in E-PCL-PS and PE-PCL-PS, and the cells were loosely sprouted toward the frame of the chamber while forming a thin cell layer, which indicates that the spheroids in the micro-chamber were not severely fused together due to the distance between the spheroids (figure 3(E)). Similarly, SEM images (figure 3(F)) confirmed that an initial shape of the four spheroids was not evident after 14 d because of aggregation while the fibers were still homogenously distributed within IPS. Instead of spheroid aggregation, the cells in E-PCL-PS and PE-PCL-PS proliferated within the holes of the chamber by filling the space.

The vertically sectioned (figure 4(A)) SEM images from PE-PCL-PS revealed that the cells began to bind with adherent strands of the chamber after 24 h, and continuously migrated, following the wall in the chamber for 14 d to form a larger tissue construct, and the initially mixed PD-FFs within the PS were observed in the central portion of the tissue (figure 4(B)). Nuclei staining of horizontally sectioned (figure 4(C)) E-PCL-PS and PE-PCL-PS demonstrated that cell migration on

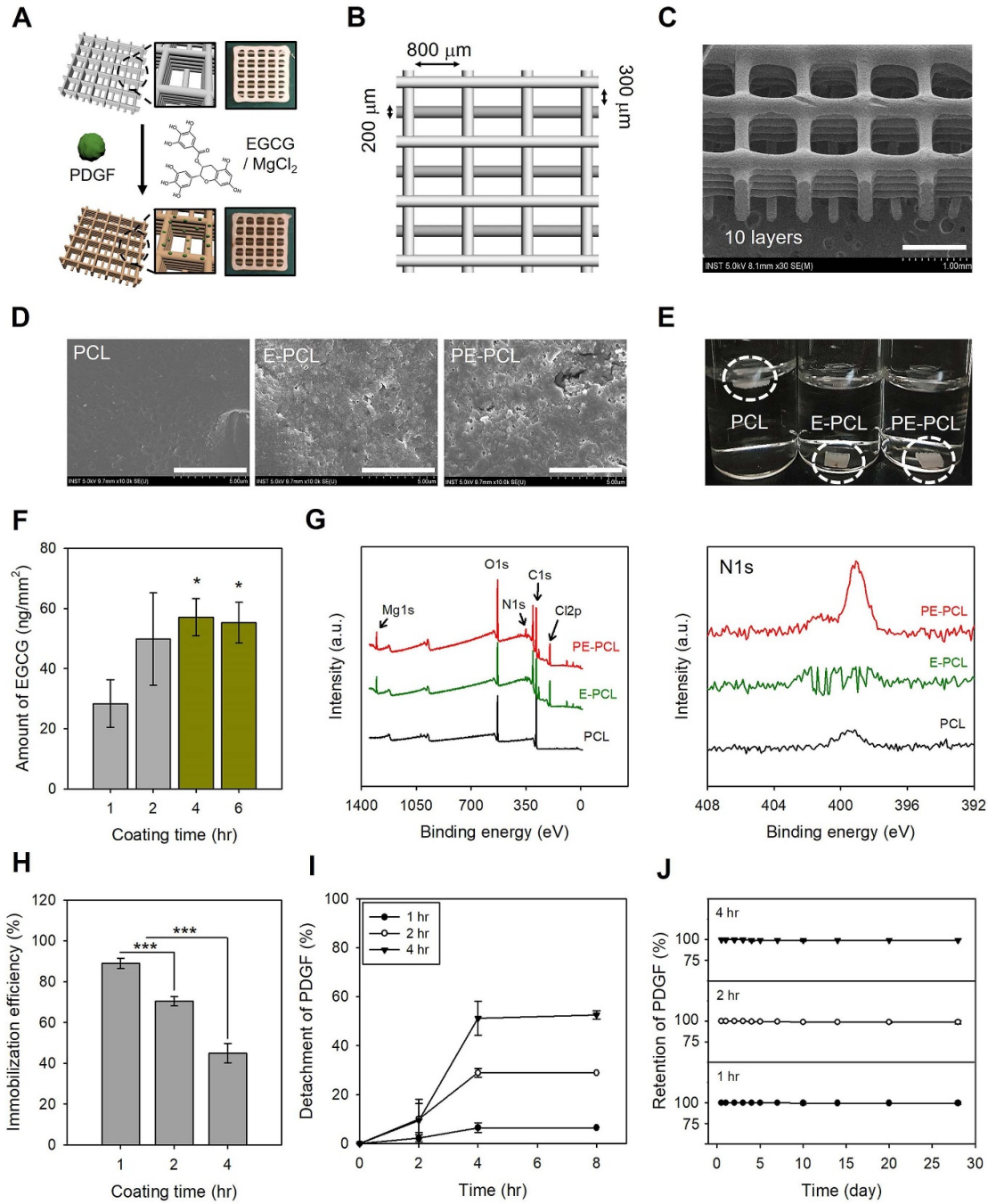

Figure 1. Characterization of EGCG and PDGF coated PCL micro-chamber. (**A**) Schematic illustration of EGCG and PDGF coating on micro-chamber, and optical image of the chambers. (**B**) 3D modeling and (**C**) SEM images of the chamber with specific size, and (**D**) high magnified SEM images of surface of PCL, E-PCL, and PE-PCL. (**E**) Optical image of the chambers dipped in distilled water. Surface chemical composition of the micro-chambers; (**F**) Amount of EGCG coated on PCL chamber depending on coating time ('*' indicates significant difference with 1 h) ($n = 5$). (**G**) XPS surface chemical composition of PCL, E-PCL, and PE-PCL analyzed by general spectra, and high magnified spectra of N1s scan. (**H**) Immobilized efficiency of PDGF on the chamber depending on coating time ($n = 5$), (**I**) detachment of PDGF from the chamber within 8 h, and (**J**) retention of immobilized PDGF from the chamber during 28 d ($n = 5$). One-way ANOVA for all statistical results ($^{*}P < 0.05$ and $^{***}P < 0.0001$).

the strands of micro-chamber was faster on PE-PCL-PS (figures 4(D) and (E)). The TUNEL assay showed that the apoptotic nuclei were distributed homogeneously around the IPS, while the nuclei were found only on the core of the spheroids at E-PCL-PS and PE-PCL-PS (figure 4(F)). Furthermore, 43.9% ± 2.4% of cells in IPS appeared to be apoptotic, and were rarely observed in cells within spheroids positioned at the micro-chambers (E-PCL-PS and PE-PCL-PS: 4.7% ± 1.6% and 0.8% ± 0.1%, respectively). In addition, PDGF coating further prevented apoptosis of hADSCs, and the number of TUNEL-positive nuclei in PE-PCL-PS was significantly lower than in E-PCL-PS (figure 4(G)). The DNA and MTT assays revealed a similar tendency of the cells within the spheroids cultured with

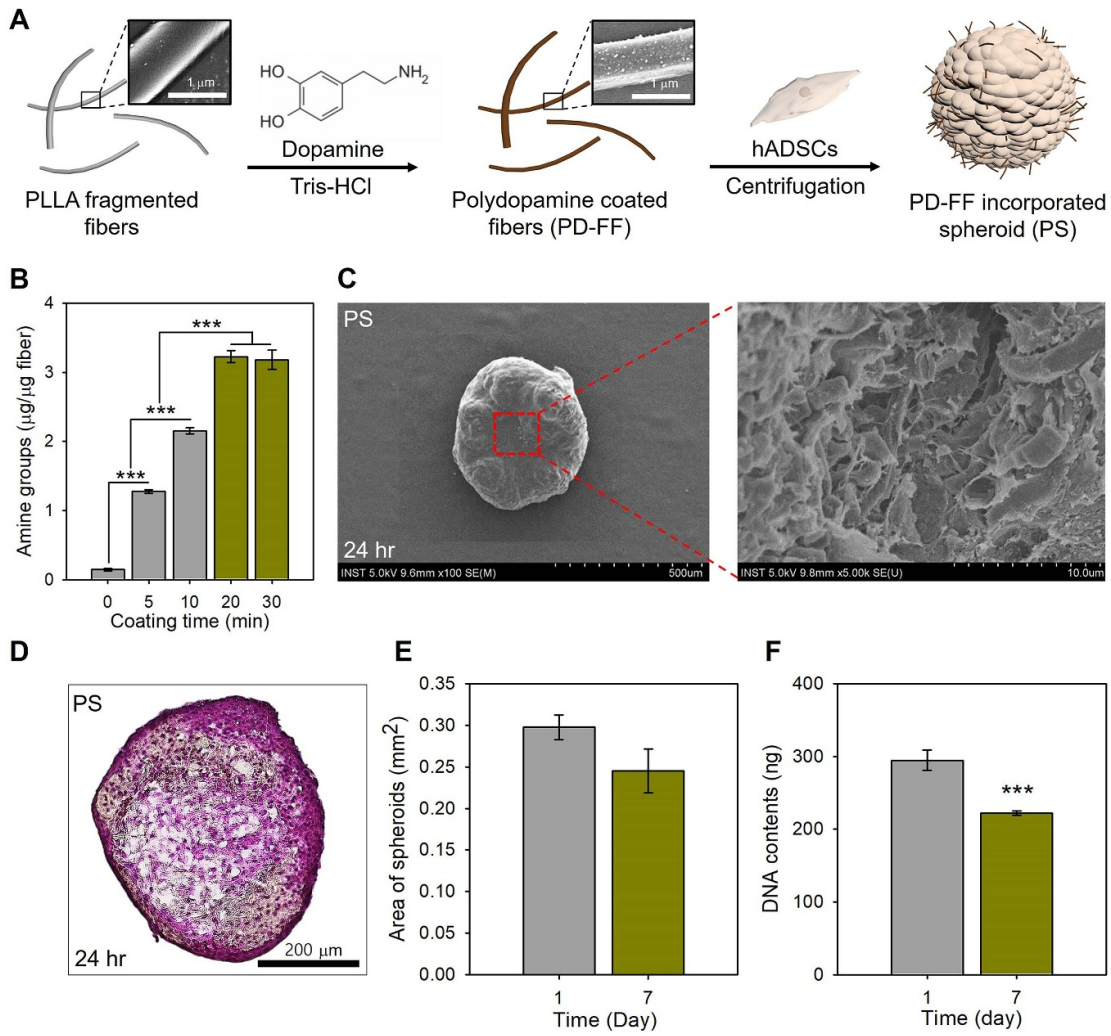

Figure 2. Preparation of spheroid with engineered fibers and hADSCs. (**A**) Schematic illustration of the method preparing the PS. (**B**) Amount of amine groups depending on dopamine coating time ($n = 5$). (**C**) SEM images of the PS with the higher magnified image of its inside. (**D**) Cross-sectioned H&E staining image of the 24 h cultured PS. (**E**) Sizes and (**F**) DNA contents of spheroids cultured for 1 and 7 d ($n = 5$). One-way ANOVA for amine quantification, and Student's T-test for DNA quantification ($^{***}P < 0.0001$).

the micro-chamber to proliferate continuously for 14 d, with the PDGF further enhancing the proliferation of stem cells. In contrast, cells cultured in the absence of the micro-chamber appeared to lose proliferative capacity (figures 4(H) and (I)). For example, the DNA contents from each group cultured for 14 d were significantly increased at 292 ± 54 ng, 1109 ± 88 ng, and 1296 ± 47 ng on IPS, E-PCL-PS, and PE-PCL-PS, respectively (figure 4(I)).

3.4. Preparation of hADSC spheroids with fibers immobilizing BMP-2

The BPS were prepared by incorporating BF50 allowing hADSCs to differentiate into an osteogenic lineage within the spheroid without osteogenic medium supplements (figure 5(a)). The immobilization efficiency of BMP-2 increased depending on two concentrations. For example, 88.5% ± 8.0% of BMP-2 was immobilized when the PD-FF was treated with 500 ng ml^{-1} of BMP-2 solution (figure 5(B)). Furthermore, BF50 showed the greatest retention of BMP-2 on fiber; 98.5% ± 2.3%, 97.0% ± 0.0%, and 92.9% ± 0.0% of BMP-2 was retained on BF50, BF30, and BF10, respectively, after 28 d (figure 5(C)). Live-and-dead staining produced few dead signals within the prepared spheroids (figure 5(D)), and H&E staining of the cross-sectioned spheroid containing BFs confirmed that the fibers and hADSCs were mixed and distributed homogeneously, and no indication of massive cell death was observed, as in the case of PS (figure 5(E)). DNA contents from the BPS were significantly enhanced to 110.6 ± 5.0% and 111.7% ± 2.2% after 4 and 7 d comparing with those of PS, respectively (figure 5(F)). RT-qPCR results demonstrated that the cells in BPS achieved gene expressions levels for RUNX2, OSX, OCN, and OPN that were 1.38 ± 0.03, 2.01 ± 0.10, 2.07 ± 0.28, and 2.50 ± 0.15 times greater, respectively, that those in PS (figure 5(G)). In addition, more calcium minerals

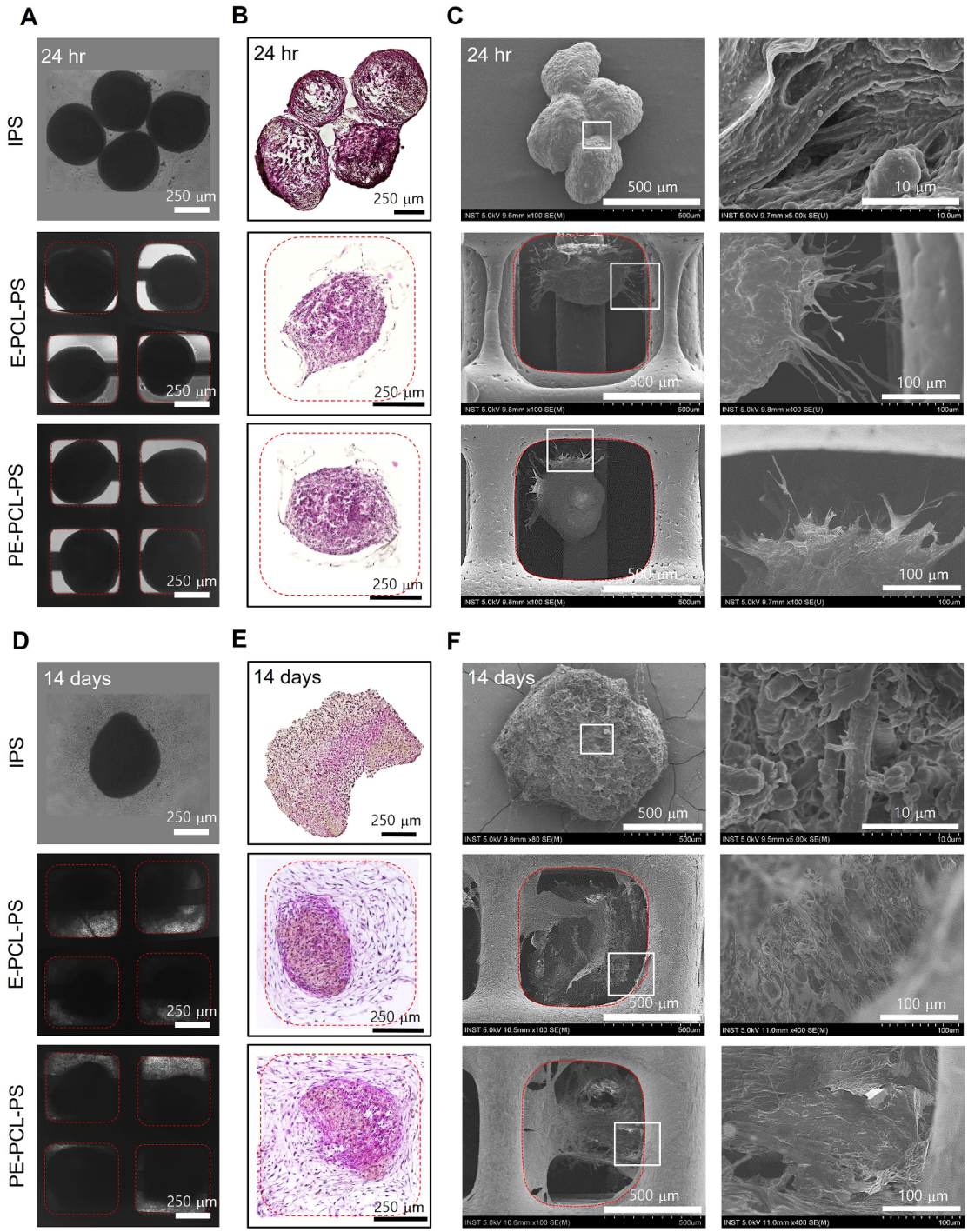

Figure 3. Characterization of the micro-chambers loaded with spheroids. (**A**) Phase contrast images, (**B**) H&E staining of horizontally sectioned samples, and (**C**) SEM images from IPS, E-PCL-PS, and PE-PCL-PS after 24 h culturing. (**D**) Phase contrast images, (**E**) H&E staining of horizontally sectioned samples, and (**F**) SEM images from IPS, E-PCL-PS, and PE-PCL-PS after culturing 14 d ('Red boxes' in histological images indicate the borderline of chamber, and 'white boxes' indicates the parts at high magnification).

were deposited on BPS than on PS (figure 5(H)), and also the section from BPS revealed intensified staining, with a reddish color for Alizarin Red S (figure 5(I)).

3.5. *In vitro* osteogenic differentiation of stem cell spheroids within 3D printed micro-chambers

We then confirmed the combined effect of PDGF coated on the 3D printed micro-chamber and BMP-2 within the spheroid on osteogenic differentiation of hADSCs *in vitro*. Overall, RT-qPCR analysis for osteogenic genes demonstrated that the cells from PE-PCL-BPS exhibited the greatest osteogenic differentiation, and the cells from E-PCL-BPS were also associated with significantly enhanced gene expression compared with those from PE-PCL-PS and E-PCL-PS, although expression was lower than with PE-PCL-BPS (figure 6). However, PE-PCL-PS

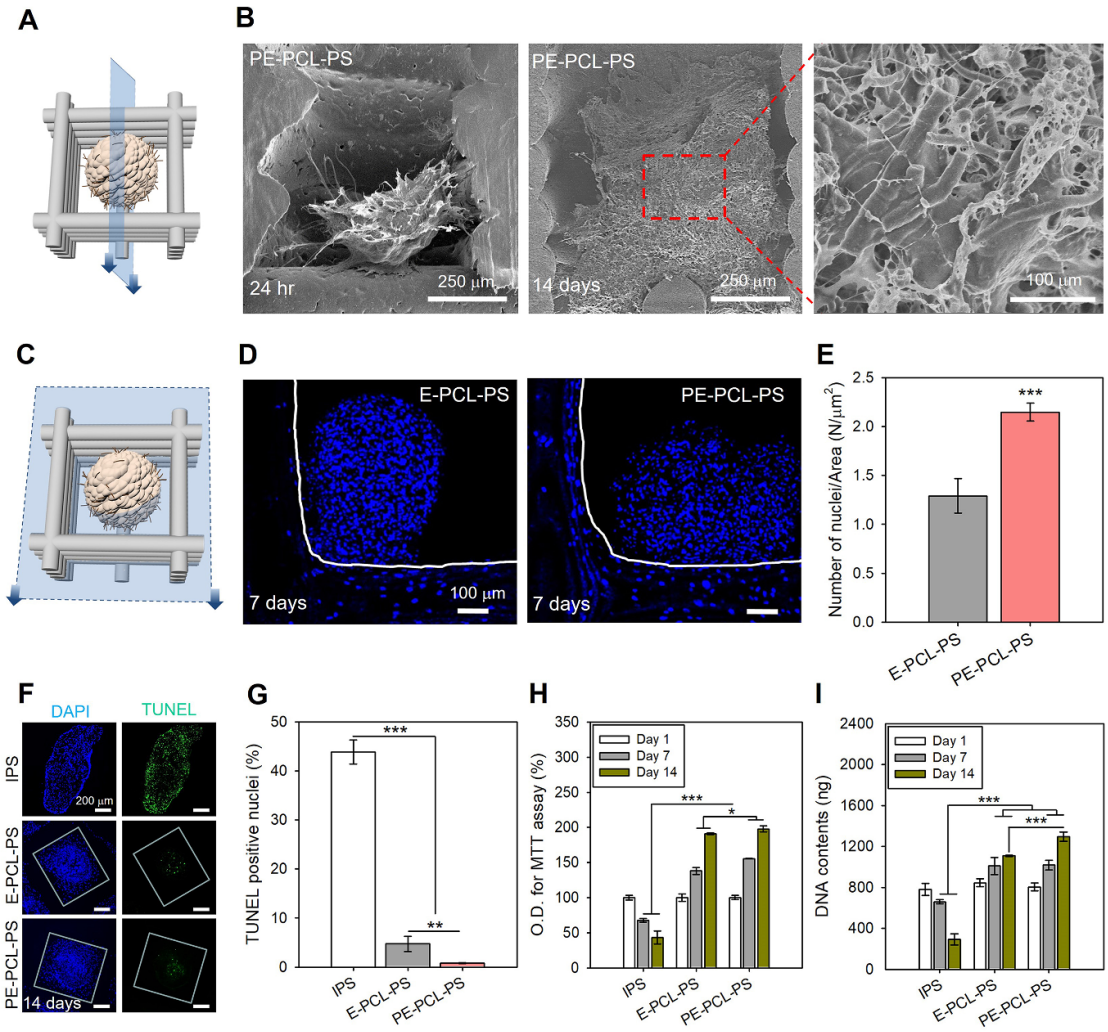

Figure 4. Proliferation of the cells from spheroids in micro-chambers. **(A)** Schematic illustration of vertical section of sample. **(B)** SEM images of vertically sectioned PE-PCL-PS being cultured for 24 h and 14 d (the portion of red box is enlarged). **(C)** The schematic illustration of horizontal section of sample. **(D)** DAPI stained fluorescent images of horizontally sectioned E-PCL-PS and PE-PCL-PS after culturing 7 d (white lines indicate borderline of chamber), and **(E)** the counted number of nuclei on chambers ($n = 5$). **(F)** TUNEL assay of IPS, E-PCL-PS, and PE-PCL-PS (white boxes indicate borderline of chamber), and **(G)** counted TUNEL positive/DAPI stained nuclei from each sample ($n = 5$). **(H)** Optical density from MTT assay and **(I)** DNA contents of IPS, E-PCL-PS, and PE-PCL-PS being cultured for 1, 7, and 14 d ($n = 5$). Student's T-test for figure 5G, and one-way ANOVA for the others ($^{*}P < 0.05$, $^{**}P < 0.001$, and $^{***}P < 0.0001$).

showed relatively reduced osteogenic gene expression that was not statistically different from E-PCL-PS (figures 6(A), (B), (C), and (D)), but greater expression for OPN and Col1a (figures 6(E) and (F)). For example, Col1a expressions from PE-PCL-PS, E-PCL-BPS, and PE-PCL-BPS were greater than that from E-PCL-PS by a factor of 5.0 ± 1.3, 27.7 ± 8.6, and 89.7 ± 0.3, respectively (figure 6(F)). The IHC staining of Col1a demonstrated that hADSCs within spheroids from E-PCL-BPS and PE-PCL-BPS groups were highly positive for Col1a while the intensity by the staining from E-PCL-PS and PE-PCL-PS group was diminished. It should be noted that the cells sprouting from the spheroid were also positive for Col1a in PE-PCL-BPS, indicating that BMP-2 effectively modulated osteogenic differentiation of hADSCs within the spheroid (figure S3). Furthermore, the staining of representative post-osteogenic differentiation markers such as OPN (figure 7(A)) and OCN (figure 7(C)) also showed tendencies similar to the results of RT-qPCR. OPN-positive signals were homogeneously distributed through the spheroid within the micro-chamber (figure 7(a)), and the numbers of OPN-positive nuclei were significantly higher in PE-PCL-BPS (51.1% ± 6.6%) and E-PCL-BPS (20.7% ± 3.5%) relative to that in PE-PCL-PS (5.8% ± 1.9%), and E-PCL-PS (4.7% ± 0.8%) (figure 7(B)). Similarly, OCN-positive signals were also homogeneously distributed (figure 7(C)) and the quantified number of nuclei showed same tendency with that of OPN staining (figure 7(D)). The ALP and Alizarin Red S staining of horizontally sectioned samples of spheroids with BMP-2 (E-PCL-BPS and PE-PCL-BPS) were

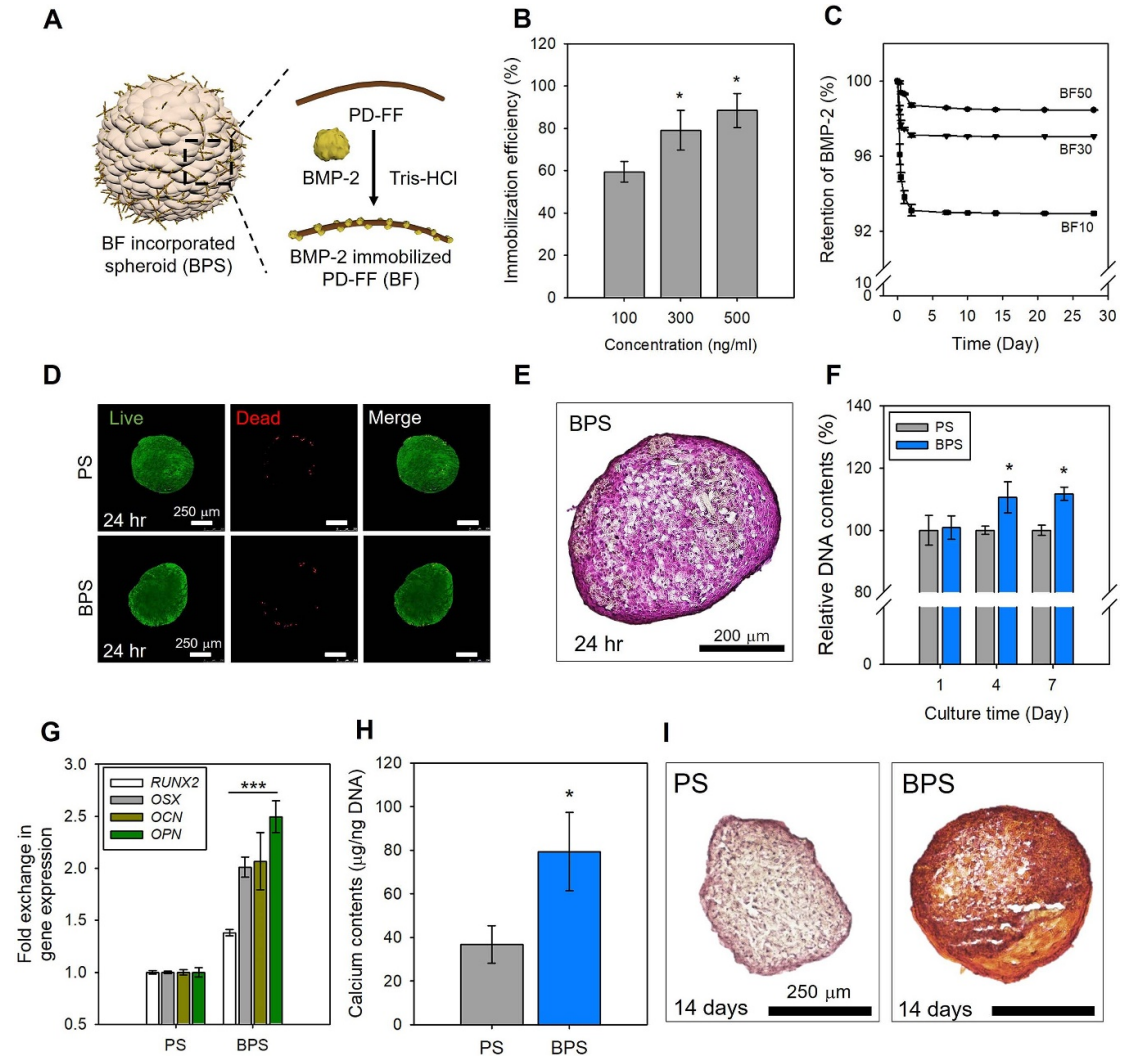

Figure 5. Characterization of BMP-2 incorporated spheroid. (**A**) Schematic illustration of the method preparing BPS. (**B**) Immobilized efficiency and (**C**) retained amount of BMP-2 onto the fibers depending on concentration of BMP-2 ($n = 5$). (**D**) Live and dead assay of PS and BPS being cultured for 24 h, and (**E**) H&E staining of horizontally sectioned BPS being cultured for 24 h. (**F**) DNA contents from PS and BPS being cultured for 1, 4, and 7 d ($n = 5$) ('*' indicates the difference between PS and BPS at each time point). (**G**) Relative osteogenic gene expressions ($n = 5$), (**H**) calcium contents, and (**I**) alizarin red S staining from PS and BPS being cultured for 14 d ($n = 5$) ('*' indicates the difference between PS and BPS). Student's T-test for all statistical results ($^{*}P < 0.05$ and $^{***}P < 0.0001$).

more violet and red than those with PS (E-PCL-PS and PE-PCL-PS), and the sample from PE-PCL-BPS produced the most intense staining compared with the other groups (figure 7(E)). As a result of calcium assay, 9.1 ± 0.6 $\mu g\ \mu g^{-1}$, 8.9 ± 0.9 $\mu g\ \mu g^{-1}$, 11.8 ± 0.0 $\mu g\ \mu g^{-1}$, and 15.3 ± 1.3 $\mu g\ \mu g^{-1}$ of DNA of calcium minerals were deposited on E-PCL-PS, PE-PCL-PS, E-PCL-BPS, and PE-PCL-BPS, respectively (figure 7(F)).

3.6. *In vivo* bone regeneration in a mouse calvarial defect model

The CSD-specific circular and cylindrical micro-chamber was designed and printed (figure 8(A)), and the spheroids were loaded onto the holes of the micro-chamber (figure 8(B)). As shown in figure 8(C), the chamber was fitted firmly to the defect without avoiding spheroids. From the micro-CT analysis, it was found that the defect, E-PCL-PS, and PE-PCL-PS groups exhibited minimal bone formation, while E-PCL-BPS groups improved bone regeneration, although the area of newly formed bone was limited to the edge of the defect. In contrast, the PE-PCL-BPS group exhibited significantly enhanced bone regeneration, with the defect well covered with newly formed bone tissue (figure 8(D)). Quantitative analysis confirmed the micro-CT results; the new bone area was 5.0% ± 1.9%, 7.6% ± 3.9%, 18.3% ± 3.2%, 32.3% ± 15.8%, and 77.0% ± 15.9% (figure 8(E)), and the BV/TV values were 0.5% ± 0.3%, 1.2% ± 1.1%, 4.5% ± 1.3%, 5.3% ± 2.0%, and 19.7% ± 5.9% for the defect, E-PCL-PS, PE-PCL-PS, E-PCL-BPS, and PE-PCL-BPS transplanted groups, respectively (figure 8(F)). As shown in Goldner's trichrome staining of

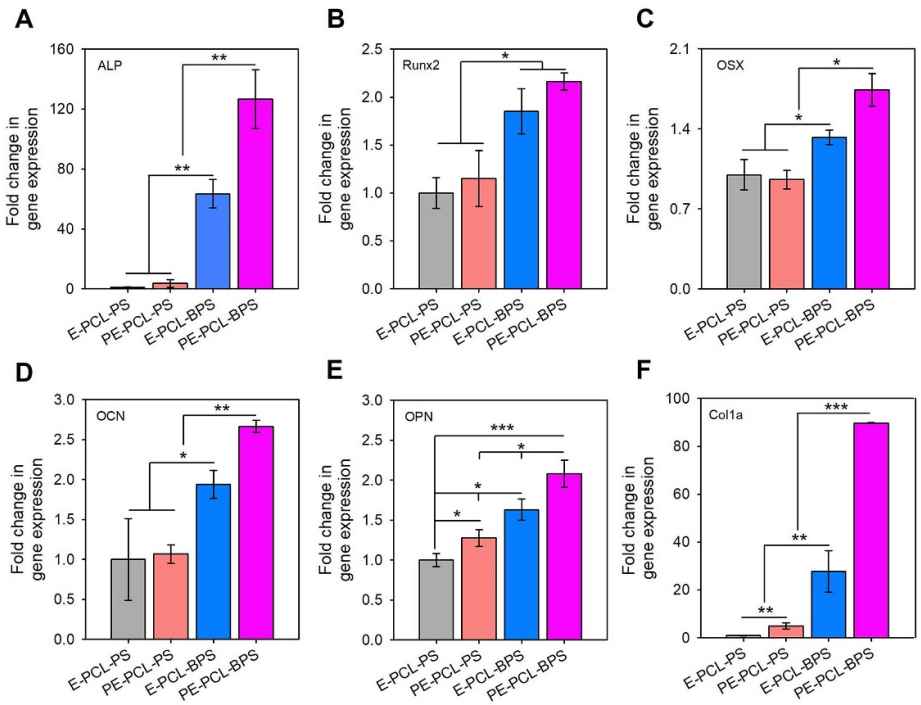

Figure 6. Osteogenic differentiation of hADSCs from the spheroids loaded on micro-chambers. Relative gene expression of **(A)** ALP, **(B)** Runx2, **(C)** OSX, **(D)** OCN, **(E)** OPN, and **(F)** Col1a for hADSCs from E-PCL-PS, PE-PCL-PS, E-PCL-BPS, and PE-PCL-BPS being cultured for 14 d ($n = 5$) ($^{*}P < 0.05$, $^{**}P < 0.01$, and $^{***}P < 0.0001$).

sectioned bone on defect site from each group (figure 8(G)), and enlarged images at parts with red boxes (figure 8(H)), the defect and E-PCL-PS groups experienced less tissue regeneration, and PE-PCL-PS acquired considerable connective tissue on the defect site. In contrast, the group transplanted with E-PCL-BPS and PE-PCL-BPS showed newly formed bone tissue with a lamellar structure (white arrow in high-magnified images), but the thickness of the tissue was greater on PE-PCL-PS while filling up the pores of the transplanted scaffold, which were observed only outside of scaffold on the E-PCL-BPS group. Furthermore, Von Kossa staining (figure 8(H)) of the regenerated tissues to which the spheroids were delivered showed that the micro-chambers with BPS (E-PCL-BPS and PE-PCL-BPS) significantly enhanced mineralization, turning a darker color while the other groups turned a bright color, indicating more minerals were deposited in the presence of BMP-2. Similarly, IHC staining of OPN (figure 8(H)) demonstrated that OPN-positive nuclei were rarely observed in the defect and E-PCL-PS groups, and were observed in PE-PCL-PS only for the spheroid-loaded area. In contrast, more cells were positive for OPN in the E-PCL-BPS and PE-PCL-BPS groups. Cells in the PE-PCL-BPS group were positive for OPN not only for the area where the spheroid was positioned but also the surrounding tissues.

4. Discussion

This study was designed to prepare 3D printed micro-chambers for carrying spheroids at regular intervals with dual growth factors. The size of a well of micro-chamber was designed as 0.8 ± 0.0 of width and 0.8 ± 0.0 of length (figure S1(B)), which was enough to hold one spheroid (0.3 ± 0.0 mm^2, figure 2(E)) to increase the accessibility of stem cells, and additional strands were aligned on the bottom of chamber to avoid the loss of spheroids as shown in figure 1. The EGCG coating rendered the surface of PCL chamber hydrophilic through oxidative polymerization, π–π stacking, and metal ion coordination (usually Na^{+} or Mg^{2+}), consistent with other studies [29, 30]. The amount of EGCG coated on the PCL micro-chamber reached a saturation point after 4 h on the micro-chamber and it was reported that the amount of EGCG reached a saturation level at a specific time depending on the size, material, and topography of scaffold [31]. The EGCG was further used for one-step surface coating of PDGF. The exact mechanism of this process has not been clearly elucidated, however, previous studies have determined that the biomolecules can be adsorbed by intervening between π–π stacking of the EGCG, forming a poly(catechin) structure through the condensation of aldehydes and phenol groups, and using hydrogen bonds and abundant hydroxyl

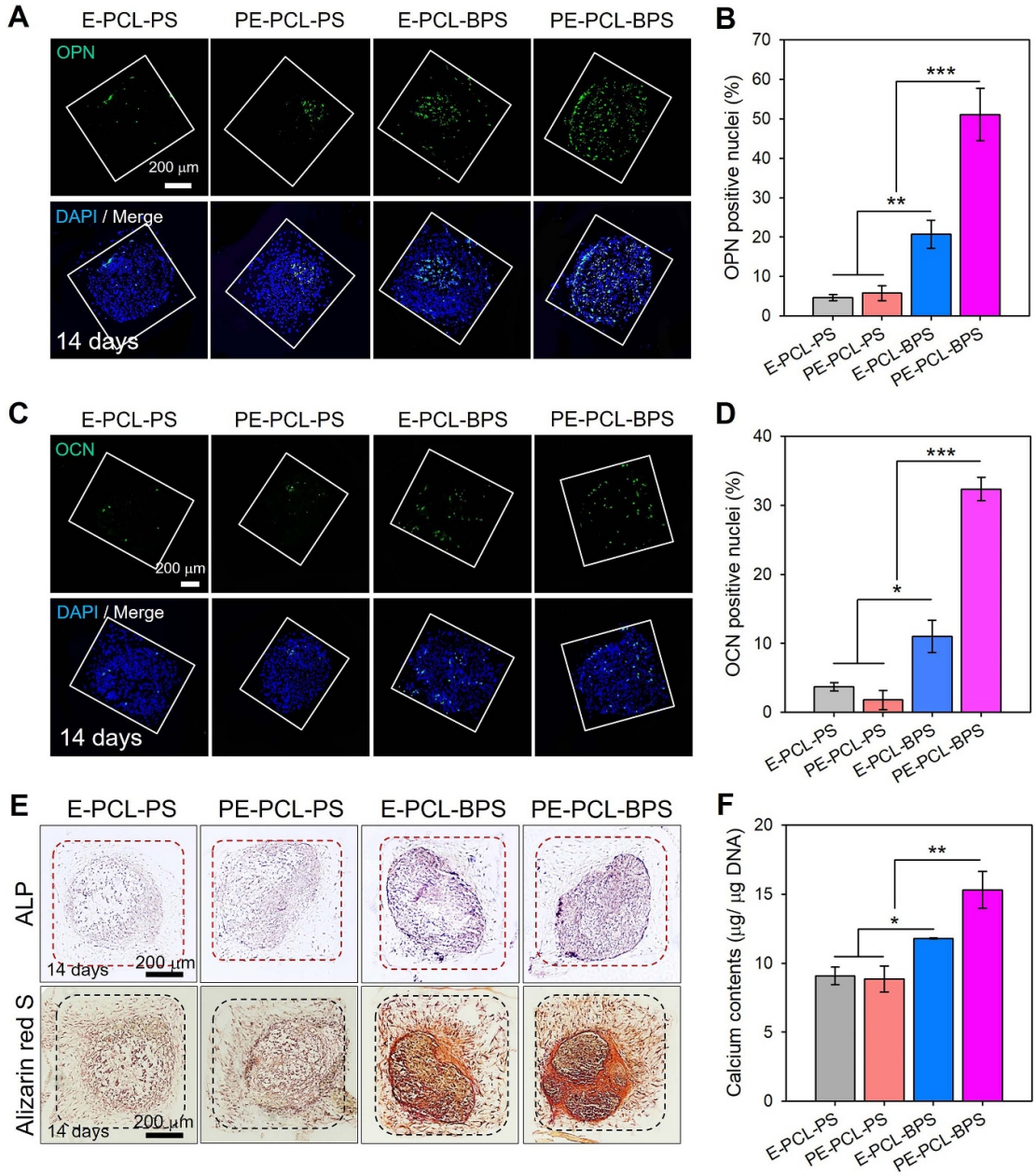

Figure 7. (**A**) IHC staining of OPN and (**B**) the number of OPN positive nuclei, and (**C**) IHC staining of OCN and (**D**) the number of OCN positive nuclei from each group ($n = 5$) (white boxes indicate borderline of chamber). (**E**) ALP and Alizarin Red S staining of horizontally sectioned E-PCL-PS, PE-PCL-PS, E-PCL-BPS, and PE-PCL-BPS. (**F**) Calcium contents from each group. One-way ANOVA for all statistical results ($n = 5$) ($^{*}P < 0.05$, $^{**}P < 0.01$, and $^{***}P < 0.0001$).

groups [32]. Interestingly, 4 h of coating reduced coating efficiency of PDGF compared with 1 and 2 h of coating (figure 1(I)). The unattached and destabilized EGCG particles may have formed a massive aggregates assembled with PDGF, which may have competed with surface immobilization process of PDGF [33]. The loosely bound PDGF on the surface of micro-chamber appeared to be detached within few hours and the remaining was retained for over 4 weeks, indicating that PDGF coating was effective by molecular intervening between π–π stacking of EGCG, leaving hydrogen bonds between hydroxyl groups of EGCG and the amine and sulfate groups of PDGF to be used for immobilization [32, 34]. The AFM results demonstrated that there were only a few nanometer differences between groups (root-mean-squared roughness (Rq) values: 7.9 ± 3.6, 19.5 ± 1.1, and 3.3 ± 0.3 nm for PCL, E-PCL, and PE-PCL, respectively). Given that, we anticipate that the EGCG and PDGF coating may not affect the spheroid attachment and migration along the strands in the micro-chamber (figure S2). In fact, the PCL originally presented flat surface, and the EGCG was also coated as homogeneously and flatly on the surface of PCL chamber which was also proved in the SEM images (figure 1(D)). Therefore, the cell adhesion on the surface was confidently more affected by the chemistry and pro-proliferative inductivity of PDGF on the

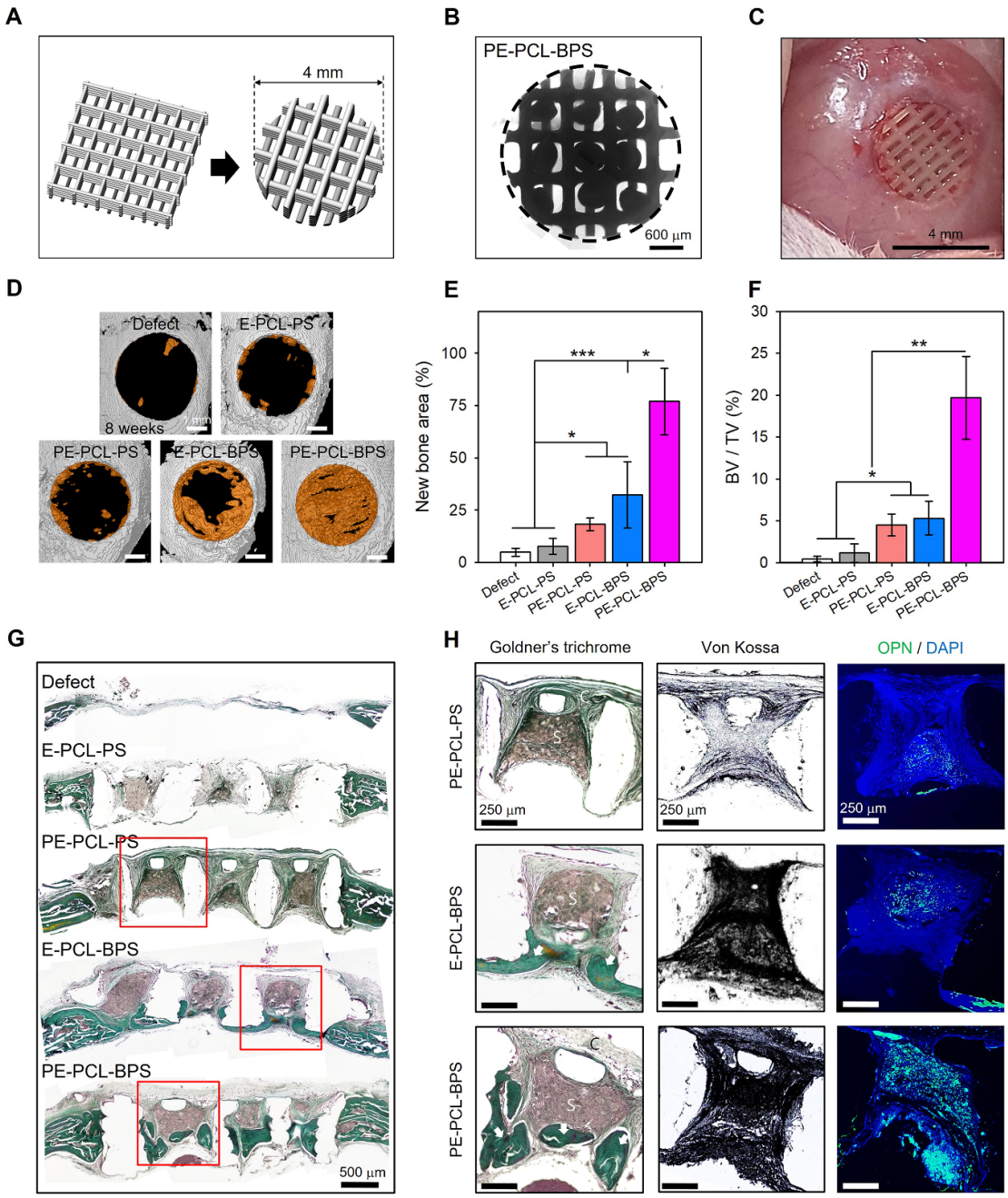

Figure 8. ***In vivo*** **implantation on mouse calvarial defect.** **(A)** Images of shape change for PCL micro-chamber through 3D modeling. **(B)** Phase contrast image of PE-PCL-BPS immediately after loading the spheroids. **(C)** Optical image of surgical procedure transplanting the chamber onto mouse calvarial defect. **(D)** Micro-CT radiographic images of calvarial defects from Defect and E-PCL-PS, PE-PCL-PS, E-PCL-BPS, and PE-PCL-BPS groups after 8 weeks ($n = 6$). Quantification of **(E)** regenerated bone coverage area and **(F)** volume from each group ($n = 6$). **(G)** Full size of cross-sectioned bone images after Goldner's trichrome staining from each group ($n = 5$). **(H)** High magnified images obtained from Goldner's trichrome staining, Von Kossa staining, and OPN IHC staining for the parts marked with red boxes ($n = 5$). One-way ANOVA for all statistical results ($^{*}P < 0.05$, $^{**}P < 0.01$, and $^{***}P < 0.0001$).

surface rather than the roughness. Furthermore, the cell adhesion and proliferation were increased in PE-PCL than E-PCL (figure 4(D)) while the roughness in nanoscale was the greater in E-PCL than PE-PCL.

In our previous study, we engineered a spheroid incorporating ECM-mimicking fibers that supplied spaces for diffusion and increased cell-ECM binding, osteogenic differentiation of stem cells with enhanced viability than a spheroid composed only of cells [27]. However, the cells in the spheroids did not proliferate and were severely condensed after 7 d, and spheroids with functional particles also exhibited similar problems in long-term culture [35]. Similar with previous studies, the PS showed condensed surface structure after 24 h and the DNA contents decreased after day 7 (figures 2(C) and (F)). The condensation is due to self-assembly of stem cells in the spheroids in the absence of an adherent surface, and such a structure may lead to differentiation of stem cells into diverse lineages. However, they may not be proliferative nor

viable because the sprouting area or opportunities for oxygen diffusion are limited [36]. The aggregation of multiple spheroids would exacerbate this phenomenon and aggregates composed of four spheroids demonstrated greater number of apoptotic nuclei (figure 4(f)). These results are consistent with previous report that larger cell aggregates exhibited significantly greater cell death rate than smaller aggregates [37]. In contrast, spheroids loaded onto a scaffold avoided condensation since cells from the spheroids attached and migrated along the strands within the micro-chamber (figure 3). As a result, the apoptotic cells in E-PCL-PS were dramatically reduced compared with those of IPS, and stem cell proliferation increased continuously during 14 d (figures 4(G), (H), and (I)). In addition to micro-chamber effects, we delivered PDGF on the surface of micro-chamber (PE-PCL-PS), which may have attributed to faster migration and proliferation, and reduced apoptosis of stem cells from spheroids compared with the group without PDGF. Taken together, our results suggest that micro-chamber with PDGF coating enhanced stem cell proliferation and migration toward the strands of chamber through ligand-receptor binding while inhibiting cell aggregation within the spheroid, which in turn can initiate the extracellular signal-regulated kinase cascade signaling pathway, leading to activation of cell division and growth factor production [38].

It has been difficult to induce spontaneous osteogenic differentiation of stem cells within spheroids by external supplements. For example, a previous study demonstrated that BMP-2–diluted medium (100 ng ml^{-1}) did not enhance osteogenic gene expression of mesenchymal stem cells within spheroids as compared to mono-layered cells [39]. The limited differentiation may be due to the diffusion limitation, such that the externally provided inductive factors enabled to interact with cells along the periphery of spheroids, but could not be permeable through densely formed cell–cell layers with difficulty in reaching cells placed in the center of the spheroid [40]. Our results showed similar histological images for both PS and BPS (figures 2(D) and 5(E)). Recently, mineralized inorganic microparticles were hybridized within spheroids to supply the osteogenic signals from inside of the spheroid [41]. For example, Wang *et al* mixed hydroxyapatite micro-particles with embryonic stem cells as spheroids, with the resulting spheroids demonstrating increase in OPN expression compared with those without particles [41]. Similarly, incorporation of calcium phosphate micro-particles within mesenchymal stem cell spheroids enhanced upregulation of osteogenic gene expression as compared to those without particles [42]. As inductive signal, we tightly immobilized the BMP-2 onto the fibers using polydopamine chemistry (figures 5(B) and (C)) and polydopamine-based immobilization of proteins on the surface of various biomaterials have been already published before [43, 44]. The immobilization with polydopamine also contributed to make the surface PLLA fibers hydrophilic, which improved homogeneous dispersion of the fibers under aqueous environment. As a result, the BMP-2 coated fibers were homogeneously mixed with cells and distributed evenly within the spheroid (figure 5(E)), and the Alizarin Red S staining of cross-sectioned BPS confirmed homogeneous differentiation stem cells within the spheroid (figure 5(I)).

The synergic effect of co-delivery of angiogenic growth factors and osteoinductive molecules for osteogenic differentiation of stem cells has been widely investigated and proved its advantages: angiogenic growth factors rapidly complete the immune response at a defect site and enhance the proliferation of stem cells and stem cells used for bone reconstruction, and then the number of being proliferated cells are directly and spontaneously differentiated and proceed to mineralization by osteoinductive molecules [45–47]. For example, Kim *et al* demonstrated that two dimensionally seeded hMSCs treated with PDGF and BMP-2 exhibited a 10-fold increase in ALP activity and calcium deposition compared with no growth factors and a 3-fold increase in activity compared with conditions in which only BMP-2 was delivered [46]. In case of spheroids, one previous study evaluated the effect of fibroblast growth factor-2 (FGF-2) with osteogenic medium for BMSC spheroids. However, the result of *in vitro* osteogenic differentiation of the spheroids showed that the FGF-2 treated group was not significantly enhanced compared with the spheroids without FGF-2 [47]. In this study, we therefore developed a new growth factor delivery system composed of rapid delivery of PDGF from the micro-chamber and continuous retention of BMP-2 from inside of the spheroid. PE-PCL-BPS showed dramatically increased osteogenic gene expression compared with an absence of growth factors and the presence of only one of them (figure 6). Moreover, Alizarin Red S staining of cross-sectioned E-PCL-BPS and PE-PCL-BPS revealed that the sprouted cells from spheroids heading for the adherent frame of the chamber were also red in color, indicating that the migrated or proliferated cells from the spheroid had differentiated into an osteogenic lineage (figure 7(E)). The mechanical compression test was performed to investigate the change of mechanical strength after spheroid loading. The average stress–strain curves of the PCL and PE-PCL-BPS (figure S4(A)) demonstrated that the micro-chamber loaded with spheroids, and PE-PCL-BPS (75.7 $\pm$ 4.0 MPa) showed significantly greater compressive modulus than PCL (61.3 $\pm$ 7.6 MPa) (figure S4(B)). Taken together, the results indicated that the spheroids loaded with the micro-chamber contributed to the increase in the mechanical properties of the construct

potentially due to filling-up of the pores by proliferating stem cells and their mineralization within the chamber, which may be more favorable for bone regeneration [48].

Despite several advantages of spheroids, delivery of the stem cell spheroids into bone defects suffers from several limitations, including abnormally bulky tissue formation and less osseointegration due to unequal distribution or aggregation of transplanted spheroids within the defect [18, 49]. In our study, the group receiving IBPS was characterized by heterogeneous results, as shown in figure S5, implying that spheroids without a scaffold may not be stably positioned or leaked after transplantation. The hydrogels carrying spheroids partially solved the leakage problem *in vivo* [19]. However, the spheroids were still movable and aggregated again in defects after hydrogel degradation because of its low mechanical property and rapid degradation compared to a scaffold with a synthetic polymer, i.e. PCL and PLGA, and the spheroids [50]. Three-dimensional bio-printing of scaffold-free spheroids using a needle with strong cell–cell interactions during the preculture step before implantation may offer a new method of delivering spheroids *in vivo*, but such applications have rarely been studied and the diffusion limitations of large, cell-based tissue constructs may decrease the therapeutic activation of spheroids and therefore limit their viability [51, 52]. In contrast to these works, in our study, with a combination of PDGF and BMP-2, the spheroids in a micro-chamber showed increased viability and proliferation compared with their aggregated form, and PE-PCL-BPS–implanted bone was associated with superior regeneration compared with the other groups. As shown in histological analysis, PDGF on the surface of a micro-chamber clearly enhanced tissue regeneration (figure 8(G)), however, most tissues from PE-PCL-PS appeared to be un-mineralized connective tissues, and were not detected by micro-CT (figure 8(D)). On the other hand, the BMP-2 within spheroids enhanced the differentiation of stem cells by receptor-ligand binding, potentially initiating SMAD signaling [46], and the affected cells rapidly may have transferred the signals to other cells through a paracrine effect [53]. As a result, the regenerated bone from E-PCL-BPS showed massive mineralized and lamellar-structured tissues (figure 8(G)). The position of lamellar structure was distinct from the spheroid area with thin cracks (figure 8(H), white arrow indicates lamella structure), indicating that the spheroid secreted osteogenic factors to adherent tissues for forming lamella structure rather than being itself. Finally, we showed that a combination of PDGF on the micro-chamber and BMP-2–incorporated spheroids (PE-PCL-BPS) can successfully produce well-organized bone regeneration (figure 8(H)). Furthermore, the lamellar structure found in PE-PCL-BPS group was positioned not only outside from spheroid, but also near the spheroid being connected without cracks (figure 8(H), white arrow on PE-PCL-BPS), which indicates the spheroids directly participated in lamella structure formation, unlike the case for E-PCL-BPS. This phenomenon could be activated by the synergistic effect of PDGF and BMP-2 further enhancing the differentiation and mineralization of spheroids.

Taken together, we prepared a new dual-growth factor delivery system by loading BMP-2 incorporated stem cell spheroids in PDGF immobilized in a micro-chamber. The results demonstrate that PDGF helps fill the defect area by enhancing the proliferation of cells from spheroids and tissue ingrowth, BMP-2 is essential for both differentiation of stem cells within the spheroid and *in vivo* mineralization of bone tissue, and the synergistic effect of PDGF and BMP-2 make effective *in vivo* osteogenesis possible using spheroids. We expect this system could offer an advance in therapeutic tool for bone regeneration as well as an effective method of delivering the spheroids.

5. Conclusion

We prepared a new dual-growth-factor delivery system by loading BMP-2–incorporated stem-cell spheroids in PDGF immobilized in a micro-chamber. *In vitro* experiments demonstrated that the viability and proliferation of stem cells from spheroids increased when cultured on a micro-chamber, and the effect was greater when PDGF coated the chamber. Our investigation of osteogenic differentiation demonstrated that PE-PCL-BPS is associated with greater differentiation compared with the other groups. In other words, the spheroid-loading chamber clearly demonstrated a synergistic effect of PDGF and BMP-2. For example, PE-PCL-BPS increased ALP and Col1a gene expression by factors of 126.7 $\pm$ 19.6 and 89.7 $\pm$ 0.3, respectively, compared with no growth factors. Finally, when the chambers were transplanted into mouse calvarial defects, bone formation was 77.0% $\pm$ 15.9% greater in the PE-PCL-BPS transplanted group. Histological analysis confirmed that PDGF enhanced tissue regeneration but was not able to induce mineralization, and BMP-2 enhanced mineralized bone-tissue formation but only at limited quantities. Meanwhile, the PE-PCL-BPS–implanted bone tissues exhibited well-organized lamellar structures with large areas. Taken together, the dual-growth-factor delivery system, which produced an initial burst of PDGF from the micro-chamber and sustained retention of BMP-2 from the inside the spheroids, could offer a new therapeutic tool for bone regeneration as well as an effective method of delivering the spheroids.

Acknowledgments

This research was supported by a National Research Foundation of Korea (NRF) grant funded by the Korean government (MEST) (Grant Nos. 2019R1A2C2084965, 2020M3H4A1A02084829, and 2020R1A4A3078645).

Author contribution

Lee J performed conceptualization, all experiments, and writing of draft, Seok J M and Park S A prepared and designed the 3D printed micro-chamber, Huh S J, Byun H, and Lee S helped characterization of spheroids and *in vivo* surgery, and Shin H designed, reviewed, edited, and supervised the project.

Conflict of interest

The all authors declare no conflict of interests.

ORCID iDs

Su A Park https://orcid.org/0000-0001-5878-8054
Heungsoo Shin https://orcid.org/0000-0002-9036-155X

References

[1] Wang C *et al* 2020 3D printing of bone tissue engineering scaffolds *Bioact. Mater.* **5** 82–91
[2] Bose S, Vahabzadeh S and Bandyopadhyay A 2013 Bone tissue engineering using 3D printing *Mater. Today* **16** 496–504
[3] Suarez-Gonzalez D, J S L, Diggs A, Lu Y, Nemke B, Markel M, Hollister S J and Murphy W L 2014 Controlled multiple growth factor delivery from bone tissue engineering scaffolds via designed affinity *Tissue Eng.* A **20** 2077–87
[4] Kirby G T S *et al* 2016 Microparticles for sustained growth factor delivery in the regeneration of critically-sized segmental tibial bone defects *Materials* **9** 259
[5] Lee H J, Koo Y W, Yeo M, Kim S H and Kim G H 2017 Recent cell printing systems for tissue engineering *Int. J. Bioprinting* **3** 27–41
[6] Jeon O, Lee Y B, Jeong H, Lee S J, Wells D and Alsberg E 2019 Individual cell-only bioink and photocurable supporting medium for 3D printing and generation of engineered tissues with complex geometries *Mater. Horiz.* **6** 1625–31
[7] Zhang M *et al* 2020 3D printing of Haversian bone-mimicking scaffolds for multicellular delivery in bone regeneration *Sci. Adv.* **6** eaaz6725
[8] Chen L, Shao L P, Wang F P, Huang Y F and Gao F H 2019 Enhancement in sustained release of antimicrobial peptide and BMP-2 from degradable three dimensional-printed PLGA scaffold for bone regeneration *Rsc Adv.* **9** 10494–507
[9] Moncal K K, Aydin R S T, Abu-Laban M, Heo D N, Rizk E, Tucker S M, Lewis G S, Hayes D and Ozbolat I T 2019 Collagen-infilled 3D printed scaffolds loaded with miR-148b-transfected bone marrow stem cells improve calvarial bone regeneration in rats *Mater. Sci. Eng.* C **105** 110128
[10] Alaribe F N, Manoto S L and Motaung S C K M 2016 Scaffolds from biomaterials: advantages and limitations in bone and tissue engineering *Biologia* **71** 353–66
[11] Zhu L S, Luo D and Liu Y 2020 Effect of the nano/microscale structure of biomaterial scaffolds on bone regeneration *Int. J. Oral Sci.* **12** 6
[12] Heller M *et al* 2016 Materials and scaffolds in medical 3D printing and bioprinting in the context of bone regeneration *Int. J. Comput. Dent.* **19** 301–21
[13] Chimene D, Miller L, Cross L M, Jaiswal M K, Singh I and Gaharwar A K 2020 Nanoengineered osteoinductive bioink for 3D bioprinting bone tissue *ACS Appl. Mater. Interfaces* **12** 15976–88
[14] Midha S, Dalela M, Sybil D, Patra P and Mohanty S 2019 Advances in three-dimensional bioprinting of bone: progress and challenges *J. Tissue Eng. Regener. Med.* **13** 925–45
[15] McKee C and Chaudhry G R 2017 Advances and challenges in stem cell culture *Colloid Surf. B* **159** 62–77
[16] Gionet-Gonzales M A and Leach J K 2018 Engineering principles for guiding spheroid function in the regeneration of bone, cartilage, and skin *Biomed. Mater.* **13** 034109
[17] Yamaguchi Y, Ohno J, Sato A, Kido H and Fukushima T 2014 Mesenchymal stem cell spheroids exhibit enhanced in-vitro and in-vivo osteoregenerative potential *Bmc Biotech.* **14** 105
[18] Suenaga H, K S F, Suzuki Y, Takato T and Ushida T 2015 Bone regeneration in calvarial defects in a rat model by implantation of human bone marrow-derived mesenchymal stromal cell spheroids *J. Mater. Sci., Mater. Med.* **26** 254
[19] Yanagihara K, Uchida S, Ohba S, Kataoka K and Itaka K 2018 Treatment of bone defects by transplantation of genetically modified mesenchymal stem cell spheroids *Mol. Ther. Methods Clin. Dev.* **9** 358–66
[20] Corstorphine L and Sefton M V 2011 Effectiveness factor and diffusion limitations in collagen gel modules containing HepG2 cells *J. Tissue Eng. Regener. Med.* **5** 119–29
[21] Lee M K, Rich M H, Baek K, Lee J and Kong H 2015 Bioinspired tuning of hydrogel permeability-rigidity dependency for 3D cell culture *Sci. Rep.* **5** 8948
[22] Hrynevich A, Elci B S, Haigh J N, McMaster R, Youssef A, Blum C, Blunk T, Hochleitner G, Groll J and Dalton P D 2018 Dimension-based design of melt electrowritten scaffolds *Small* **14** e1800232
[23] McMaster R *et al* 2019 Tailored melt electrowritten scaffolds for the generation of sheet-like tissue constructs from multicellular spheroids *Adv. Healthcare Mater.* **8** 1801326
[24] Daly A C and Kelly D J 2019 Biofabrication of spatially organised tissues by directing the growth of cellular spheroids within 3D printed polymeric microchambers *Biomaterials* **197** 194–206
[25] Lee S J, Lee D, Yoon T R, Kim H K, Jo H H, Park J S, Lee J H, Kim W D, Kwon I K and Park S A 2016 Surface modification of 3D-printed porous scaffolds via mussel-inspired polydopamine and effective immobilization of rhBMP-2 to promote osteogenic differentiation for bone tissue engineering *Acta Biomater.* **40** 182–91
[26] Ahmad T, Lee J, Shin Y M, Shin H J, Perikamana S K M, Park S H, Kim S W and Shin H 2017 Hybrid-spheroids incorporating ECM like engineered fragmented fibers potentiate stem cell function by improved cell/cell and cell/ECM interactions *Acta Biomater.* **64** 161–75
[27] Ahmad T, Byun H, Lee J, Perikamana S K M, Shin Y M, Kim E M and Shin H 2020 Stem cell spheroids incorporating fibers coated with adenosine and polydopamine as a modular building blocks for bone tissue engineering *Biomaterials* **230** 119652
[28] Samsonraj R M, Dudakovic A, Zan P F, Pichurin O, Cool S M and van Wijnen A J 2017 A versatile protocol for studying calvarial bone defect healing in a mouse model *Tissue Eng.* C **23** 686–93
[29] Sileika T S, Barrett D G, Zhang R, Lau K H A and Messersmith P B 2013 Colorless multifunctional coatings inspired by polyphenols found in tea, chocolate, and wine *Angew. Chem., Int. Ed.* **52** 10766–70

[30] Qian Y, Yao Z X, Wang X, Cheng Y, Fang Z W, Yuan W E, Fan C Y and Ouyang Y M 2020 (-)-Epigallocatechin gallate-loaded polycaprolactone scaffolds fabricated using a 3D integrated moulding method alleviate immune stress and induce neurogenesis *Cell Proliferat.* **53** e12730
[31] Peter B, Farkas E, Forgacs E, Saftics A, Kovacs B, Kurunczi S, Szekacs I, Csampai A, Bosze S and Horvath R 2017 Green tea polyphenol tailors cell adhesivity of RGD displaying surfaces: multicomponent models monitored optically *Sci. Rep.* **7** 42220
[32] Saeki K, Hayakawa S, Nakano S, Ito S, Oishi Y, Suzuki Y and Isemura M 2018 *In vitro* and in silico studies of the molecular interactions of epigallocatechin-3-O-gallate (EGCG) with proteins that explain the health benefits of green tea *Molecules* **23** 1295
[33] Wu S S, Sun K, Wang X, Wang D X, Wan X C and Zhang J S 2013 Protonation of epigallocatechin-3-gallate (EGCG) results in massive aggregation and reduced oral bioavailability of EGCG-dispersed selenium nanoparticles *J. Agr. Food Chem.* **61** 7268–75
[34] Shim A H R, Liu H L, Focia P J, Chen X Y, Lin P C and He X L 2010 Structures of a platelet-derived growth factor/propeptide complex and a platelet-derived growth factor/receptor complex *Proc. Natl Acad. Sci. USA* **107** 11307–12
[35] Abbasi F, M H G, Baharvand H, Vahidi B and Eslaminejad M B 2018 Engineering mesenchymal stem cell spheroids by incorporation of mechanoregulator microparticles *J. Mech. Behav. Biomed.* **84** 74–87
[36] Sart S, Tsai A C, Li Y and Ma T 2014 Three-dimensional aggregates of mesenchymal stem cells: cellular mechanisms, biological properties, and applications *Tissue Eng.* B **20** 365–80
[37] Jung H R *et al* 2017 Cell spheroids with enhanced aggressiveness to mimic human liver cancer *in vitro* and in vivo *Sci. Rep.* **7** 10499
[38] Mihaylova Z, Tsikandelova R, Sanimirov P, Gateva N, Mitev V and Ishkitiev N 2018 Role of PDGF-BB in proliferation, differentiation and maintaining stem cell properties of PDL cells *in vitro Arch. Oral Biol.* **85** 1–9
[39] Miyaguchi N, Kajiya H, Yamaguchi M, Sato A, Yasunaga M, Toshimitu T, Yanagi T, Matsumoto A, Kido H and Ohno J 2018 Bone morphogenetic protein-2 accelerates osteogenic differentiation in spheroid-derived mesenchymal stem cells *J. Hard Tissue Biol.* **27** 343–50
[40] Cui X, Hartanto Y and Zhang H 2017 Advances in multicellular spheroids formation *J. R. Soc. Interface* **14** 20160877
[41] Wang Y, Yu X H, Baker C, Murphy W L and T C M 2016 Mineral particles modulate osteo-chondrogenic differentiation of embryonic stem cell aggregates *Acta Biomater.* **29** 42–51
[42] Zarkesh I, Halvaei M, Ghanian M H, Bagheri F, Sayahpour F A, Azami M, Mohammadi J, Baharvand H and Eslaminejad M B 2020 Scalable and cost-effective generation of osteogenic micro-tissues through the incorporation of inorganic microparticles within mesenchymal stem cell spheroids *Biofabrication* **12** 015021
[43] Lynge M E, van der Westen R, Postma A and Stadler B 2011 Polydopamine-a nature-inspired polymer coating for biomedical science *Nanoscale* **3** 4916–28
[44] Huang S S, Liang N Y, Hu Y, Zhou X and Abidi N 2016 Polydopamine-assisted surface modification for bone biosubstitutes *Biomed. Res. Int.* **2016** 2389895
[45] Xie H *et al* 2014 PDGF-BB secreted by preosteoclasts induces angiogenesis during coupling with osteogenesis *Nat. Med.* **20** 1270–8
[46] Kim J and Hollinger J O 2014 Effects of dual delivery of rhPDGF-BB and rhBMP-2 on osteogenic differentiation of human mesenchymal stem cells *Tissue Eng. Regener. Med.* **11** 143–8
[47] Tae J Y, Ko Y and Park J B 2019 Evaluation of fibroblast growth factor-2 on the proliferation of osteogenic potential and protein expression of stem cell spheroids composed of stem cells derived from bone marrow *Exp. Ther. Med.* **18** 326–31
[48] Cho Y S, Quan M L, Kang N U, Jeong H J, Hong M W, Kim Y Y and Cho Y S 2020 Strategy for enhancing mechanical properties and bone regeneration of 3D polycaprolactone kagome scaffold: nano hydroxyapatite composite and its exposure *Eur. Polym. J.* **134** 109814
[49] Annamalai R T, Hong X W, Schott N G, Tiruchinapally G, Levi B and Stegemann J P 2019 Injectable osteogenic microtissues containing mesenchymal stromal cells conformally fill and repair critical-size defects *Biomaterials* **208** 32–44
[50] Oyen M L 2014 Mechanical characterisation of hydrogel materials *Int. Mater. Rev.* **59** 44–59
[51] Ayan B, Heo D N, Zhang Z, Dey M, Povilianskas A, Drapaca C and Ozbolat I T 2020 Aspiration-assisted bioprinting for precise positioning of biologics *Sci. Adv.* **6** eaaw5111
[52] Arai K, Murata D, Verissimo A R, Mukae Y, Itoh M, Nakamura A, Morita S and Nakayama K 2018 Fabrication of scaffold-free tubular cardiac constructs using a Bio-3D printer *PloS One* **13** e0209162
[53] Petrenko Y, Sykova E and Kubinova S 2017 The therapeutic potential of three-dimensional multipotent mesenchymal stromal cell spheroids *Stem Cell Res. Ther.* **8** 94